Development of Image-Based Beam Model for Assessment of Osteoporotic Hip Fracture Risk

By

Huijuan Yang

A thesis submitted to
the Faculty of Graduate Studies
in partial fulfilment of
the requirements for the degree of
Master of Science

Department of Mechanical Engineering
Faculty of Engineering
University of Manitoba
Winnipeg, Manitoba

March 2017

Abstract

Hip fracture has been identified as a major worldwide health problem among the elderly population. A fast, accurate and effective evaluation of hip fracture risk is essential for accurate health care planning and selecting a proper treatment. Therefore, the high applicability and the universal availability are required for assessing a technique. The objective of this study was to develop a two-dimensional subject-specific beam model, which is easy to be adopted into a clinical environment to assess hip fracture risk.

First, the equivalence between CTXA (computed tomography X-ray absorptiometry) and QCT (quantitative computed tomography) derived femur cross-section stiffness was studied. Then, the CTXA-based femur cross-section stiffness was used in the beam model to calculate the hip fracture risk index (FRI) during sideways fall and single-leg stance loading configuration. Finally, the test of discrimination between PPI (proton-pump inhibitor) users and non-PPI users based on cross-sectional stiffness, BMD (bone mineral density) and FRI was conducted to demonstrate if PPI use is associated with the presence of osteoporosis or accelerated BMD loss.

Strong correlation is found between CTXA and QCT derived femur cross-section stiffness, which indicates that QCT can be replaced by CTXA in assessing femur bone quality. Therefore, DXA can be a replacement of QCT to calculate femur cross-sectional properties due to the equivalence between CTXA and DXA derived mechanical properties. It is also demonstrated that the cross-sectional stiffness, BMD, and FRI cannot discriminate the PPI users from non-PPI users, which means that there is no difference between PPI users and non-PPI users in cross-sectional

stiffness, BMD, and FRI. This may suggested that PPI use is not associated with the presence of osteoporosis or accelerated BMD loss. The proposed beam model can be easily adopted into clinic to predict hip fracture risk, and this beam model derived FRI can be used in some clinical verification. Yet its accuracy of discriminate fracture will be investigated in a future study.

Acknowledgements

I would like to take this opportunity to express my sincerest thanks to a number of people. First, I would like to thank my supervisor, Dr. Yunhua Luo, for his patient guidance, encouragement and advice throughout this work. I have been so lucky to have a supervisor who has been so influential in ensuring my academic, professional, financial, and moral well-being, which will be always appreciated.

Many thanks goes to the advisory committee members, Drs. I. Telichev and Y.-J. Cha, for their time spent in evaluation the thesis and for their constructive advice.

I would like to express my gratitude to the Winnipeg Health Science Center for providing the clinical cases in this study.

I would also like to thank my dear friends in Winnipeg as well as my colleagues in the Computational Biomechanics Group for all the academic discussion, mutual support, encouragement, and happy time working together.

I would like to express my deep love and appreciation to my parents, sister and brother for their unconditional love and support through my life. Finally, my special thanks to my husband, my son and my daughter for their love, understanding, and supporting during the past two years.

Dedication

To my parents, husband, and my son and daughter

Contents

Front matter

List of Tables

List of Figures

List of Copyrighted Material

Figure 1.2 was cited from "Hip Fractures in Adults". The permission was obtained on November 30th, 2016.

List of Symbols

A	Area of the section
ave_p_value_CTXA	Average pixel value in ROI area of the femoral neck in CTXA image
E	Elastic modulus
e	The square of the difference between the actual bone mineral density and the estimated bone mineral density
e'	The sum of the square of the difference between the actual bone mineral density and the estimated bone mineral density
E_i	Elastic modulus of *ith* pixel or voxel
F_h	Reaction force on head
F_{impact}	Impact force in sideways fall
F_k	Reaction force on the knee
F_{load}	Loading force in one-legged stance
G	Shear modulus
H	Body height
I	Moment of inertia
J	Torsional constant
K_a	Axial stiffness
K_{a_CTXA}	Axial stiffness in CTXA images

K_{a_QCT}	Axial stiffness in QCT images
K_b	Bending stiffness
K_{b_CTXA}	Bending stiffness in CTXA images
K_{b_QCT}	Bending stiffness in QCT images
K_s	Shear stiffness
K_{s_CTXA}	Shear stiffness in CTXA images
K_{s_QCT}	Shear stiffness in QCT images
K_t	Torsional stiffness
N	Total numbers of the pixels
P	Probability of statistical significance
p_value_CT	Pixel value in CT image
p_value_CTXA	Pixel value in CTXA image
r	Correlation coefficient
U	Strain energy
U_a	Strain energy induced by axial force
U_b	Strain energy induced by bending moment
U_s	Strain energy induced by shear force
U_Y	Yield strain energy
W	Body weight
y_i	The distance of the *ith* pixelto the mid-axis of the image
y_{i_c}	The distance of the *ith* pixel to the centroid of the bone mass distribution in the profile

y_{i_CTXA}	The distance of the *ith* pixel to the mid-point of the cross-sectional line in CTXA images
ε_Y	Yield strain
η_{hfri}	The fracture risk index
ρ_a	Areal bone mineral density
$\rho_{a\_estimated}$	Estimated average areal bone mineral density of the ROI area
ρ_{a_QCT}	Average areal bone mineral density of the ROI area based on QCT PRO software
ρ_b	The fully mineralized bone density
ρ_i	Bone mineral density of each pixel or voxel
ρ_v	Volumetric bone mineral density
$\rho_{v\_estimated}$	Estimated average volumetric bone mineral density of the ROI area
ρ_{v_QCT}	Average volumetric bone mineral density of the ROI area based on QCT PRO software
ρ_{vi}	Volumetric bone mineral density of i-th pixel
σ_Y	Yield stress
σ_{Yi}	Yield stress of the *i-th* pixel
υ	Poison ration
Δ	The pixel spacing along the profile line

List of Abbreviations

2-D	Two-dimensional
3-D	Three-dimensional
aBMD	Areal Bone Mineral Density
AUC	Area Under the ROC Curve
BMC	Bone Mineral Content
BMD	Bone Mineral Density
CSA	Cross-sectional Area
CSMI	Cross-Sectional Moment Inertia
CT	Computed Tomography
CTXA	Computed Tomography X-ray Absorptiometry
DXA	Dual-Energy X-ray Absorptiometry
FE	Finite Element
FEA	Finite Element Analysis

FHA	Femoral Head Apex
FN	Femoral Neck
FNA	Femoral Neck Axis
FNSA	Femoral Neck-Shaft Axis Angle
FRAX®	Fracture Risk Assessment Tool
FRI	Fracture Risk Index
FS	Femoral Shaft
FSA	Femoral Shaft Axis
FSL	Femoral Shaft Length
FUC	Field Uniformity Correction
HAS	Hip Structure Analysis
HU	Hounsfield Unit
IT	Intertrochanter
LSR	Load-Strength Ratio
NFN	Narrowest Femoral Neck
PPI	Proton Pump Inhibitor
QCT	Quantitative Computed Tomography

ROC	Receiver Operating Characteristic
ROI	Region of Interest
SM	Section Modulus
vBMD	Volumetric Bone Mineral Density
WHO	World Health Organization

Chapter 1

Introduction

1.1 The Prevalence of Hip Fracture and the Significance of Accurately Assessing Hip Fracture Risk

Hip fracture has been recognized as a significant public health problem and a major cause of suffering, disability, and death in the elderly [1, 2]. The mortality rates are 20-24% in the first year after a hip fracture [3, 4], and a greater risk of death may persist for at least 5 years afterwards [5]. Among the survivors, 40% are unable to walk independently, and 60% still require assistance even one year later [6].

The vast majority of hip fractures are related to both accident fall and osteoporosis [7, 8]. Osteoporosis is a skeletal disease characterized by substantial reduction in bone mass, which resulting in the increasing of bone fragility and hence susceptibility to fracture [9]. Osteoporotic fracture (fractures associated with osteoporosis) are more common than heart attack, stroke and breast cancer combined. The lifetime risk of osteoporosis fractures is 33% in women and 20% in men [10]. In the United States alone, it is estimated that 2 million osteoporotic fractures occur

annually [11]. In Canada, over $2.3 billion was spent on osteoporosis fracture in 2010, and this cost will rise to $3.9 billion if considering the long-term care facilities due to osteoporosis [12]. Among osteoporotic fractures, hip fractures has the highest morbidity and mortality, and more attention has been focused on hip fracture other than other osteoporotic fractures [13]. In terms of falls, hip fractures are the most serious fall injuries. More than 95% of osteoporotic hip fractures are caused by accident fall. Usually, sideways falls are more likely to cause hip fractures in contrast to forward or backward falls [14]. During a sideways fall, hip fracture risk is increased by 6-fold compared with backward or forward fall and 30-fold if the hip is directly impacted [15].

According to statistic studies, the population is aging significantly around the world, and the incidence rate of hip fractures is exponentially increased with age [7]. The peak number of hip fractures occurred at 75-79 years of age for both sexes. At age 50, lifetime risk of fractures is 1:2 in women and 1:5 in men [1]. Of all hip fractures, women account for nearly 75% [16]. Globally, the total number of hip fractures will dramatically rise from 1.66 million in 1950 to 3.94 million in 2025, and to 6.26 million in 2050, without considering the age- and sex-specific incidence (Figure 1.1) [17]. Even based on a conservative projection, the number of hip fractures will reach 21.3 million by 2050 [17, 18]. As shown in Figure 1.1, the striking increases are expected to occur in Asian. In the United States alone, the number of hip fractures will climb from 238,000 in 1986 to 512,000 in 2040. With the aging rate becoming even faster, the number of hip fracture will reached 840,000 by 2040 [19]. In Canada, more than 30,000 hip fractures occur each year, and this number will be quadrupled by the year 2030 [20-22].

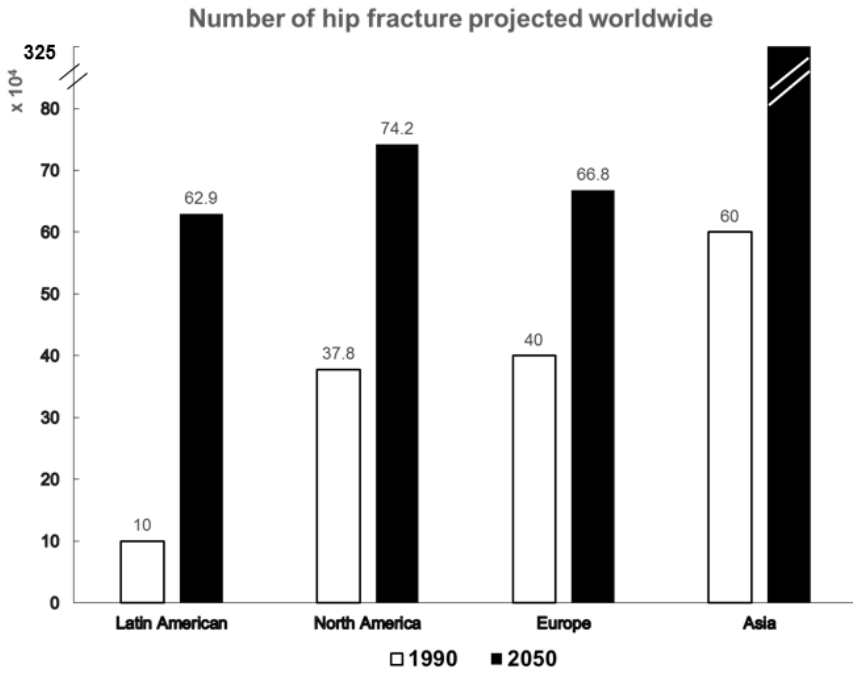

Figure 1.1 Regional distribution of hip fracture occurring in 1990 and 2050. (Total number of hip fractures worldwide projected to increase 3 to 4 fold from 1990 to 2050: 1990=1.66 million; 2050=6.26 million)[17]

Consequences of hip fractures are significant in terms of the economic cost because hip fractures are more likely to cause prolonged hospitalization and rehabilitative care. According to Lauritzen [23], almost fifty percent of the patients with hip fractures have become more dependent, and one in five will live in a nursing home. Each hip fracture costs the medical-care system $21,285 in the 1st year after hospitalization, and $44,156 if the patient is institutionalized [24]. In 1984, the estimated number of the cost of hip fracture and related care in the United States is $7.2 billion or an average of $29,800 per hip fracture. If a modest 5% inflation rate is assumed, the total annual cost for hip fracture care will rise to $62 billion by 2020 and $240 billion by 2040 [19]. The overall yearly medical expenditure for the treatment of osteoporotic hip fractures in Canada was over $2.3 billion as of 2010. This cost rises to $3.9 billion under the assumption that a proportion of Canadians lived in long term facilities due to osteoporosis [25].

Another important aspect related to hip fractures is the effect of injury on a person's life independence, decreased quality of life and depression, especially in older people [26]. After a hip fracture, the happiness of their life is reduced enormously. Only a minority of the patients can reach the same level of functioning as before fracture (personal care and daily activities) [27]. Most people have to experience a long recovery period, or be referred to a rehabilitation facility. Twenty percent of the patients suffer from severe pain. People who previously were able to live independently will generally need help [26]. More emotional distress, more feeling of loneliness and worse general health are founded among them [27].

Due to the prevalence, high medical costs, and the related social problems of hip fractures, early identification of high-risk patients and prevention of hip fracture are critical. Therefore, it is extremely important to accurately assess hip fracture risk for osteoporosis patients and discriminate the high-risk hip fracture patients to put them in an intervention program to prevent future fractures.

1.2 Hip Fracture Types

A hip fracture is a partial or complete break in the upper quarter of the femur bone. Anatomically, a hip consists of a ball-and-socket join, where the top of the femur and part of the pelvic bone meet together. The ball is the head of the femur and the socket is the curved part of the pelvic bone called the acetabulum. The primary function of hip is to support the weight of the body in both static and walking postures [28]. A hip fracture may occur at different site of the ball portion (femur) of the hip joint. Generally, it can be classified into three major categories, depending on the location of the fracture: femoral neck fractures, intertrochanteric fractures, and subtrochanteric fractures, as shown in Figure 1.2 [29]. According to Michelson et al, 49 percent are

intertrochanteric fractures, 34 percent are femoral neck fractures, and 14 percent are subtrochanteric fractures respectively [30].

Femoral neck fractures normally occur in the narrowest section of the upper femur which is between the femoral head and the trochanter [31]. These fractures can be further subdivided into subcapital and transcervical neck fractures as shown in Figure 1.2. A femoral neck fracture is usually accompanied by tearing the blood vessels passing through the femoral neck region. Therefore, femoral neck fractures may cut off the blood supply to the femoral head, resulting in more healing complications such as fractures non-union, or femoral head necrosis. In this kind of fracture, hip replacement is recommended. However, if it is just a small or nondisplaced fracture, an internal fixation is suggested to treat the fracture [31].

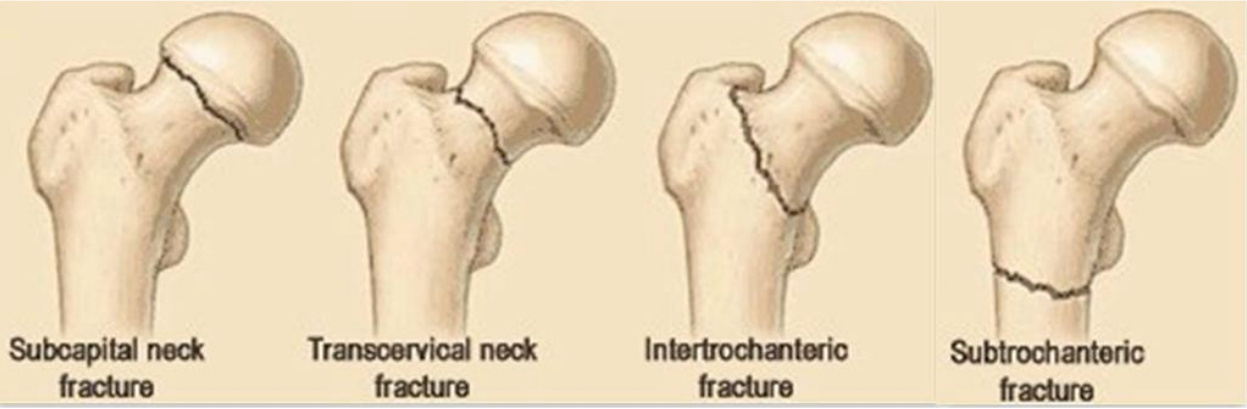

Figure 1.2 Three major types of hip fractures: femoral neck fractures (including subcapital and transcortical fractures), intertrochanteric fractures, and subtrochanteric fractures [29].

Intertrochanteric fractures occur below the femoral neck, in the area between the greater and sub-trochanter. This type of fracture does not stop blood flow to the femur, and may be easier to repair. Generally, stabilization is involved in the treatment of intertrochanteric fractures. However, these fractures are complicated due to the considerable forces induced by the attached

muscles. Therefore, the treatment more likely causes shortening of the femoral length or healing of the fracture with a misaligned position [31].

A subtrochanteric fractures normally occurs in the proximal portion of the femur shaft. Subtrochanteric fractures are less common than the other two fractures mentioned above. However, the torsional effects caused by the attached muscles and the high stresses from the daily activities make this type of fracture difficult to fix.

1.3 Existing Techniques for Assessing Hip Fracture Risk and Their Limitations

1.3.1 BMD Method

Currently, bone mineral density (BMD) is a well-established method for in vivo osteoporosis risk assessment. It is the most popular way to evaluate bone quality and fracture risk. A highly significant correlation has been shown between BMD and bone strength [32]. The risk of fracture increases exponentially as BMD decreases, therefore, BMD is a powerful predictor of fracture risk [32].

There are several ways to measure bone mineral density, and the best known is Dual-Energy X-ray Absorptiometry (DXA), which is regarded as the “gold standard” by the World Health Organization (WHO) for the diagnosis of osteoporosis due to its low dosage of radiation, high precision, and fast scan [33]. During a DXA scan, two types of X-rays with different level of energy are employed to determine the bone mineral content (BMC), then, areal bone mineral density (aBMD, g/cm^2) is derived by dividing BMC by the area of region of interest (ROI). The

aBMD is converted into T-score and Z-score. T-score compares the patient's aBMD with that of the healthy young adults of the same sex. Z-score compares the patient's aBMD with the mean aBMD derived from the reference group with same age, sex, and ethnicity. The difference between the patient's bone density and the average of the reference group is converted to standard deviations away from the mean value, called T-score [32]. The BMD diagnosis is based on the WHO diagnostic classification (see Table1.1). However, there are some limitations if only rely on the WHO categories to determine fracture risk. First, the fracture risk assessed by a given category can substantially vary at different ages [34]. For example, a 90-year-old woman with osteopenia is expected to have a higher fracture risk than a 60-year-old woman with osteoporosis. However, based on the WHO categories, the 60-year-old woman will be screened to have the osteoporosis treatment. Second, the BMD only tells bone density, other factors such as the ongoing change of the bone density, the bone type, and other factors are not considered. For example, BMD doesn't give the information that if you are currently losing bone or if you have already had low bone density for a long period; BMD measures all body types the same way and doesn't consider that a thinner woman will always has a lower bone density than a heavier woman [35]. Also, the accuracy of BMD measurement to assess hip fracture risk is limited. The placement of patient on the machine causes a 5-6% change from test to test [35].

Table 1.1 Definition of normal, osteopenia, osteoporosis and severe osteoporosis by WHO

T-score	Diagnosis
T-score>=-1	Normal bone density(low fracture risk)
-2.5<T-score<-1	Osteopenia (intermediate fracture risk)
T-score<=-2.5	Osteoporosis(high fracture risk)

1.3.2 FRAX®

Fracture Risk Assessment Tool (FRAX®) was issued by WHO in 2008 to evaluate a patient's 10-year probability of hip fracture in order to provide general clinical guidance for treatment decisions [36]. In addition to BMD at the femoral neck measured by DXA, FRAX® also incorporate other personal information called non-BMD clinical risk factors to estimate risk and probability of fracture in the next 10 years [37]. This information can help the doctor decide whether further action needs to be taken. The non-BMD clinical risk factors include sex, age, body mass index (BMI), fracture history, glucocorticoid history, current smoking, alcohol intake, etc. Compared to BMD method, FRAX® provide a more accurate method to assess fracture risk. However, it also has limitations. First, the fracture probability varies considerably among different countries in the world, thus, it may become complicated to determine intervention threshold by the fracture probabilities [38]. Also, FRAX® does not take into account fall-induced impact force in the assessment of fracture risk. Impact force on the hip is considered as a critical factor since most hip fractures are caused by sideways falls and the impact force directly acts on the trochanter of the hip [39]. Fall-related parameters may be applied in FRAX® in the future, but the data collection need to be done in a systematic way, and the best performance should be achieved by data validation.

1.3.3 Hip Structure Analysis (HSA)

Hip Structural Analysis (HSA) was developed to improve the prediction of fracture risk using hip bone mineral density incorporated with structural parameters derived from DXA scan [40]. The derived structural parameters include section modulus, cross-sectional moment of inertia, mean cortical thickness, etc. [41]. All of those structural parameter can be calculated via HSA software,

which is now commercially available. HSA program measures both the BMD of the hip bone and structural geometry of cross-sections traversing the proximal femur. The method is based on the principle that in a DXA image, a line of pixels orthogonal to the bone axis is a projection of the corresponding cross-section in the 3-D QCT image and contains some information of the cross-section, such as the geometry [41]. Although some research reported that HAS predicted strength is more precisely than aBMD method [40], there are limitations. First, HSA program employs 2-D DXA scans to extract cross-sectional properties at certain locations on femur, however, DXA scanners were not designed to measure geometry. Small changes in femur rotation will result in large effect on the projected dimensions, and the inconsistent femur position alters projected dimensions. As a result, the real dimensional differences cannot be distinguished from projection error and the results are more operator-dependent [42, 43]. The second limitation of HSA is that edge margins are difficult to locate precisely in noisy and blurred scan images [41]. The measurement accuracy is dependent on image quality. Finally, HSA program is still more complex than it should be due to the calculation of the unfamiliar geometric properties, such as Neck-Shaft Angles, Endocortical Dimater, Femoral Shaft Average Cortical Thickness, etc. For the clinical practice, it still needs many assumptions to simplify [41].

1.4 The Advantages of Biomechanical Modeling

Osteoporotic hip fracture is associated with many risk factors, and it is difficult and almost impossible to study all of these factors. Strictly speaking, in order to measure bone strength, the most reliable and direct way is to conduct destructive mechanical testing. However, it is impractical for in vivo diagnosis [41]. Therefore, it is required to use methods or models to non-invasively estimate the risk of hip fracture. Though the methods mentioned above including BMD,

FRAX, and HSA, etc. can predict the risk of hip fracture from different risk factors, they have limitations and the accuracy needs to be improved. Furthermore, their common limitation is that they have not considered hip geometry and loading conditions.

In biomechanics, the risk of osteoporotic hip fracture is decided by the load-strength ratio (LSR), which is calculated by the applied load divided by the bone strength [44-46]:

$$\text{LSR}=\frac{\textit{The applied load}}{\textit{The bone strength}}$$

Where the applied load is usually the impact force induced in a bump or fall, and the bone strength, which is determined by bone quality and bone geometry based on the theories of material mechanics and strength, is the allowable force that the bone can sustain without fracture [45].Therefore, from the engineering point of view, to better evaluate the risk of fracture, at least three major biomechanical factors need to be considered which include impact force (loading condition), bone quality and geometry. Recently the applications of biomechanical models in computer simulations, which incorporate structural dimensions, knowledge of the loading condition, and the material properties, to predict the risk of hip fracture have progressed rapidly. Obviously, it is more reasonable and accurate in predicting hip fracture risk compared to the other methods. Among these biomechanical models, finite element modelling based on medical images is considered a promising technique [47].

1.5 Objective

The objective of this study is to develop a highly applicable and universally available two-dimensional subject-specific beam model to assess hip fracture risk. To achieve this objective, the equivalence between CTXA- and QCT-derived femur cross-section stiffness is first studied. The

results can partially justify the use of DXA in replacement of QCT in assessing femur bone quality. Then, a CTXA-derived subject-specific beam model is developed, which is easier to be adopted into clinical environment, to assess hip fracture risk, and the CTXA-derived femur cross-section stiffness (bending stiffness (EI), axial stiffness (EA), and shear stiffness (GA)) are combined with this beam model to calculate hip fracture risk index (FRI) for sideways fall and single-leg stance loading configurations. Finally, the beam model is applied in a clinical validation to study if PPI use is associated with the presence of osteoporosis or accelerated BMD loss.

1.6 Outline of This Thesis

After highlighting the motivation and the objectives of this project in this chapter, the rest work will be organized as follows:

Chapter 2 – In this chapter, hip fracture evaluation using biomechanical model will be first reviewed. Then, currently popular methods to predict the fracture risk, including QCT- and DXA-based finite element models, will be introduced. Finally, image-based beam model will be presented.

Chapter 3 – In this chapter, anatomic structure of hip and the cross-sectional mechanical properties will be introduced. Then, QCT- and CTXA-based cross sectional stiffness will be calculated. During the calculation, data extraction from image, derivation of the coefficient between pixel value and BMD, and the correlation analysis between aBMD and vBMD will be presented.

Chapter4 – In this chapter, CTXA-based beam model will be constructed based on the data extracted from CTXA image. HFRI based on the cross-section strain energy will be calculated under the two common loading conditions: single-leg stance configuration and sideways fall.

Chapter 5 – In this chapter, the correlation between QCT- and CTXA-based cross-sectional stiffness will be analyzed, and the verification that DXA-based cross-sectional stiffness can substitute QCT-based cross-sectional stiffness will be provided. The test of discrimination between PPI users and non-PPI users based on cross-sectional stiffness, BMD and FRI was conducted to demonstrate if PPI use is associated with the presence of osteoporosis or accelerated BMD loss.

Chapter 6 – In this chapter, the major conclusions and contributions from this study will be summarized. Future research work will be recommended to minimize the limitations in the current research.

Chapter 2

Literature Review

2.1 Review of Hip Fracture Risk Evaluation Using Biomechanical Models

Biomechanical models apply mechanical laws to living structures, especially to the musculoskeletal system of the body based on biomechanical principles and theories [48]. They are used to predict the mechanical behaviours of an object using its shape, structure and material property information. These models can be constructed from different medical images. From the engineering point of view, a hip fracture is a structural failure, where the loads applied on the femur exceed the femur strength. This "load-to-strength ratio" approach provides insight into development of effective assessment tools. In theory, a model integrating mass distribution, structural geometry and patient-specific loading should be more accurate for assessment of hip fracture risk [49]. In this regard, a biomechanical measure may better evaluate hip fracture risk and improve fracture risk assessment [46].

For bone stress analysis, the most promising biomechanical model is finite element analysis (FEA) model, which can model the irregular geometry and heterogeneous bone [50]. The finite element method is an advanced computational method for structural stress analysis, which was introduced to orthopedic biomechanics in 1972 to evaluate stresses in human bones [51]. Since then, FEA has been widely used to study human bone mechanics [52]. Finite element (FE) models incorporate information of the femoral bone structural geometry and bone material properties derived from medical images and simulated loading conditions leading to fractures. Since 1990s, FE modeling has been increasingly used to specifically assess hip fracture risk due to the availability of newly invented digital imaging techniques [53, 54]. Recently, with the development of computer hardware and software tools, substantial progress in the application of FEA was made and the era of patient-specific FE modeling began [55]. Right now, the commercially available software such as ANSYS, ABAQUS or in-house computer codes developed using MATLAB, C, etc. are commonly used in FEA.

Generally, the implemented image-based FE models are divided into two categories, three-dimensional and two-dimensional models constructed from either CT or DXA images. For example, Testi et al. [56] and Buijs et al. [57] developed a two dimensional finite element model from DXA image and the projection of quantitative computed tomography (CT) scans, respectively. For three dimensional models, Keyak et al. [58] and Viceconti et al. [59] used CT images to build the three dimensional model; Cody et al. [60], however, derived the three dimensional model from QCT image. Their basic steps using FE modeling to assess hip fracture risk include extracting the femoral geometry from the medical image, generating a finite element mesh, assigning the material properties, applying the loading conditions, and implementing the finite element analysis. All of these models have their limitations and characteristics. Based on

literature review above, QCT-based three dimensional and DXA-based two dimensional models are the two main FE models in the current research. Therefore, in the following sections, QCT-based three dimensional and DXA-based two dimensional finite element models will be reviewed.

2.2 QCT-based Finite Element Models

Over the past 20 years, when the faster computers became available, a number of FEA models of QCT scans of human femur have been developed to assess bone mechanical characteristics, including bone strength, stress, strain, failure load, fracture location and hip fracture risk [61-64].

There are three stages in QCT-based FEA for hip fracture risk evaluation. The first step is generation of the 3-D FE model from the QCT images of femoral bone. In this step, the CT data acquisition, the region of interest (ROI) segmentation and mesh generation need to be processed based on the QCT images. In order to obtain a high quality and accurate FE model, mesh generation is one of the main issues. Generally, the mesh generation techniques include voxel based mesh and geometry based mesh [61]. After the 3-D FE model is constructed, material properties of the each element in the model is assigned. Bone density in each element is defined based on Hounsfield unit (HU) value. According to the equations between bone density and mechanical properties, Young's modulus in the element is defined as well [61]. Because bone stiffness is highly connected to material properties, the assignment of accurate material properties to the model is critical. It is preferable to represent inhomogeneous property over the entire bone. The final step is to apply the loading and boundary conditions, simulating the single-leg stance or the sideways fall configuration. A number of commercial software such as ANSYS, ABAQUS or in-house developed computer codes are available to use. The steps are summarized in Figure 2.1.

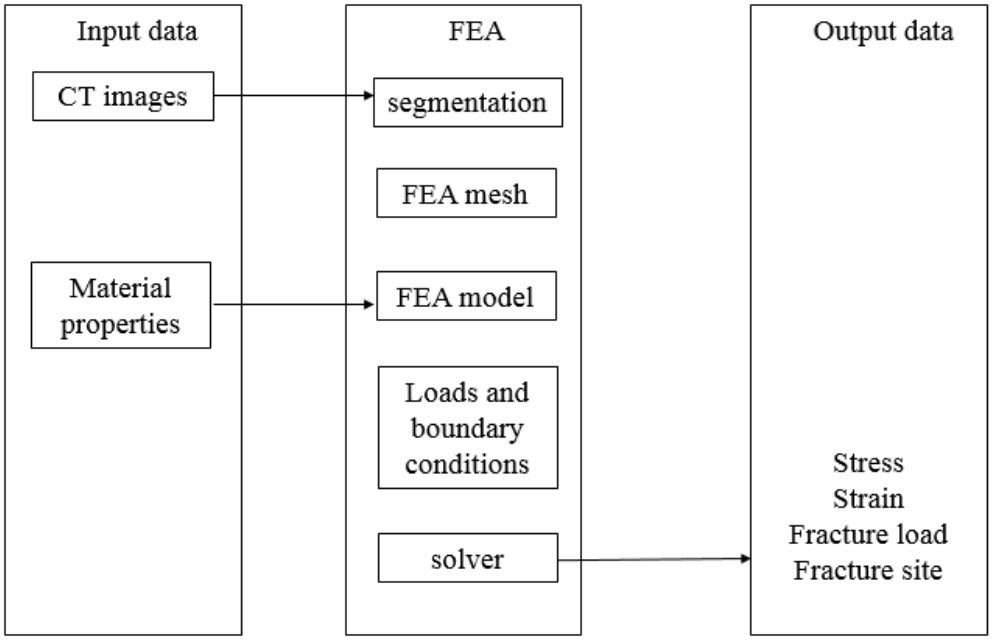

Figure 2.1 Steps involved in QCT-based FEA for hip fracture risk assessment

Although QCT-based 3-D FEA has been recognized as a prospective and reliable tool, there are some limitations. One major problem is they are time-consuming and computationally expensive, therefore, they are difficult to be applied to clinical studies. For example, linear FE models have taken up to 6–8 hours [60] while non-linear models can take approximately 10 hours for each case [65, 66]. Second, the high X-ray dosage required to acquire the quality images may be a potential health concern, and QCT scans are not routinely performed in the clinical procedure. Third, it is quite complex in respect to the 3-D model construction and the material properties assignment, and its accuracy relies on meshes or elements. Therefore, more universally available and simpler tools are preferred for clinical applications.

2.3 DXA-based Finite Element Models

Currently, DXA images are commonly used to derive two dimensional FE models used to assess hip fracture risk. Due to the low radiation dosage of X-ray, short computational time, and low-cost screening technique for obtaining bone properties relevant to strength compared to 3-D imaging modalities, DXA-based 2-D FEA is likely to be more clinically feasible and is more useful for routine hip fracture predictions on a large number of patients. Based on literature, a number of DXA-based FE models were developed to evaluate hip fracture risk in the past few years [47, 67, 68].

The general procedure to construct a DXA-based FE model is similar to the construction of a QCT-based 3-D FE model. The main difference is the DXA-based FE model is from the two dimensional DXA image, and the resulting model is 2-D geometry of the femur bone. Compared to the QCT-based 3-D FE model, DXA-based 2-D FE model is simpler in contour segmentation, mesh generation and assignment of material properties. However, the accuracy of prediction of hip fracture is possibly compromised. Actually, a number of studies have sought to improve the predictions of hip fracture risk by DXA-based 2-D FEA method. After proposing a DXA-based patient-specific finite element modeling procedure to improve the accuracy of the hip fracture assessment [47], Luo et al. focused to identify the factors that have dominant effects on the precision of the procedure in his later research paper [68].

Whereas, there are some issues need to be addressed in DXA-based 2-D FEA method. First, restricted by the two-dimensional feature of DXA scans, DXA-based 2-D FE models lack the depth information of the 3-D object and the resolution of the structural dimension is also low, which may affect the accuracy of predicted hip fracture risk. In addition, a number of assumptions are made

to evaluate bone strength from 2-D DXA data and how well the simplified 2-D model represents the original 3-D FE model is not known [69]. Furthermore, a high stress is generated on the shaft because the boundary conditions are applied on the distal end of the femur in simulating the real world forces. These stresses increase the fracture risk, but it is not realistic risk since the applied boundary conditions cannot faithfully simulate real world force configuration. Finally, it still highly depend on the model construction, mesh generation and is still technically complicated for routine clinical application.

2.4 Beam Models

From a biomechanical viewpoint, FEA is a powerful and accurate tool to evaluate hip fracture risk due to the incorporation of bone geometry, material properties and loading conditions. However, its accuracy relies on the quality of mesh or elements. According to van Rietbergen et al. [70], a realistic FE model of proximal femur requires tens of millions of elements and hundreds of hours [71]. Therefore, the complexity of the procedure, the time-consuming calculation and the high costs for quality scanners limit their clinical applicability and their use in large-scale research studies [69]. The simplicity of beam model, on the other hand, may be better suited to evaluate bone strength, especially considering the practical limitations of clinical measurements. Also, a beam model can directly output cross-sectional stiffness which can be used to evaluate bone quality and hip fracture risk. Beam models have been shown reasonable accuracy to predict stress in the femoral shaft and are considerably less expensive in computational resources [72].

A beam model is an engineering model in which an object is simulated as a loaded beam. Mathematically, it is much simpler than a FE model. The earliest idea that using beam theory to analyze the stresses in bones was proposed by Koch in 1917 [73]. In a beam model, the femur

bone with a slender shape is treated as a supporting beam with various cross-sectional properties continuously varying along its length, and its mechanical behaviour can be approximately described. A beam model can be constructed from either DXA or QCT image. Although three-dimensional beam models have been proved to better approximate the hip geometry, the complex geometry of the proximal femur does not contribute too much to the accuracy [73, 74]. In addition, the limitations of QCT image in clinical practice also make the 3-D beam model less applicable. Therefore, a 2-D beam model will be useful in assessing hip fracture risk. Generally, a DXA-based 2-D beam model is preferable since DXA technique is still widely available in clinical practice.

The first step to construct a 2-D beam model is to generate the geometry of the femur bone from a DXA image, which can be done with in-house MATLAB codes. The geometry generation includes tracing the edges, locating critical cross-sections (normally narrowest femoral neck, intertrochanter, and the femoral shaft) and the center of femoral head, determining neck and shaft axes, and detecting the neck-shaft angle. Material properties can be converted from the pixel values contained in the DXA image based on empirical equations. According to physiological loading conditions, stresses generated by physiological forces are mainly axial, bending and shearing stresses [41]. Therefore, the cross-sectional parameter such as cross-sectional area (CSA) and the cross-sectional moment inertia (CSMI) are then calculated from DXA scans, based on the projection principle that a line of pixel values across femur bone contains information of bone mass distribution [41]. After that, the loading and boundary conditions, simulating single-leg stance or sideways fall configuration, are applied to the constructed beam model. Finally, the mechanical responses of femur cross-section such as stresses, stiffness and strain energy are calculated to predict fracture risk.

A number of 2-D beam models have been developed recently, including curved beam model, curved composite beam model, and straight beam model [75, 76]. Among those beam models, the one developed by Thomas J. Beck is already applied in clinics [40, 76]. However, there are some problems in this model. First, only cross-sectional moment of inertia (CSMI) is considered in evaluating bone rigidity [40], which actually cannot represent femur stiffness without considering material properties. Secondly, the effective bone thickness of femur cross-section is calculated by the quotient of bone mass and bone density, the latter is considered as a constant (i.e. the density of fully mineralized bone tissue, 1.85g/cm^3). Considering the highly heterogeneity of bone tissues, it is not reasonable. Finally, this beam model is constructed from a two-dimensional DXA image. If it can represent the three-dimensional beam model, which can much better simulate the real femur bone, was not investigated.

In this project, a simpler straight two-dimensional beam model is developed which only consider the femoral neck and shaft as the parts of the beam under the goal that it is easier to be adopted into clinical environment. In this beam model, the bending stiffness, axial stiffness, and shear stiffness (the information required for calculating the torsional stiffness is missing due to the two-dimensional image of CTXA) are employed to describe the ability of femur bone to withstand loading instead of only considering moment of inertia, the geometry property of the femur bone. Furthermore, the effective thickness of the cross-section for calculating the geometry properties (cross-section area (CSA), cross-section moment inertia (CSMI)) is obtained by dividing areal bone mineral density by volumetric bone mineral density, which is more case specific. Finally, the equivalence between CTXA- and QCT- (2-D and 3-D) derived stiffness parameters is studied in this beam model, which gives a clear idea that if CTXA can be used in replacement of QCT in assessing femur bone quality.

Chapter 3

Cross-sectional Mechanical Properties of Femur Derived from Medical Images

3.1 The Relation among QCT-, DXA- and CTXA-based Mechanical Properties

The CTXA-Hip module in QCT PRO software (Mindways, Texas, USA) can generate bone projection images through 3-D QCT volume data sets. This projection images visually looks like that generated by clinical DXA. Based on reported research [77, 78], CTXA Hip provides substantially the same clinical information as conventional DXA. According to Cann, etc., CTXA Hip BMD is highly correlated with that measured by DXA, and CTXA is equivalent to DXA [77]. Therefore, if mechanical properties from CTXA images are equivalent with those from QCT images, there should exist high correlations between DXA and QCT derived mechanical properties, which means DXA can be a replacement of QCT to calculate femur cross-sectional properties.

Therefore a beam model of femur can be constructed from clinical DXA, which is more practical in clinical use.

3.2 Anatomical Structure of Femur

The femur is the longest and also the strongest bone in the human body and it is between the hip joint and the knee joint .The main function of the femurs is to support the weight of the upper body and allows the motion of the lower extremities. The femur has three parts: the shaft, the proximal and distal portions.

The proximal portion is composed of femoral head, femoral neck, greater trochanter, and less trochanter. The femoral head is smooth, spherical shape, which forms the ball-and-socket hip joint with the cup-shaped acetabulum of the hip bone. The femoral neck is an approximate cylindrical bone, connecting the femoral head with the femoral shaft. The angle between femoral neck and shaft is about 120 to 130 degrees. At the end of the femoral neck, the greater and lesser trochanters serve as points of attachment for several ligaments and tendons of the buttocks and thighs [79]. The shaft of the femur is roughly cylindrical in shape, and its upper part is a little thicker than its center part. The long shaft is not straight but slightly arched as it descends toward the knee, which allows the knee joint to be closer to the body's center of gravity and provide for a better balance [80]. The distal portion of the femur has round, smooth medial and lateral condyles, which meet with the condyles of the tibia to form the articular surface of the knee joint.

Based on literature [31], hip fracture most likely happens at one of three locations: femoral neck, intertrochanter, and subtrochanter. Therefore, attention has been focused on the mechanical properties of the three critical cross-sections of the femur.

3.3 Cross-sectional Mechanical Properties of Femur

The mechanical properties of a material or structure describe its responses to an applied load. The most common properties include stiffness, strength, hardness, etc. From an engineering perspective, the mechanical properties and loading are the two factors governing material damage and structural fracture. For a structure, the mechanical properties are affected by both the material properties and the geometric shape. As discussed in the previous section, the most common locations of hip fracture are femoral neck, intertrochanter and subtrochanter. Bone is an anisotropic and inhomogeneous material, and the femur bone could be simplified as an engineering beam. Therefore, the cross-sectional stiffness of femur are considered to be the most important mechanical properties affecting hip fracture.

3.3.1 Axial, Shear, Bending and Torsional Stiffness of Femur

Generally, the stiffness, including axial stiffness (K_a), beading stiffness (K_b), shear stiffness (K_s) and torsional stiffness (K_t), are used to describe the ability of an engineering beam to withstand, respectively, axial force, bending moment, transversal force, and axial torque. For a homogeneous beam cross-section, the stiffness parameters are calculated as

$$K_a = EA, \quad K_b = EI, \quad K_s = GA, \quad K_t = GJ \tag{3.1}$$

Where *E* and *G* are the elasticity modulus and shear modulus, respectively. *I* represents the bending moment of inertia of the section, *A* is the area of the section. *J* is the polar moment of inertia. It should be noted that the information required for calculating the torsional stiffness is missing in a two-dimensional image. In order to do the correlation analysis between 3-D- and 2-D- image based

cross-sectional stiffness, the torsional stiffness will not be considered. As can be seen from Equation (3.1), the stiffness parameters are affected by both the cross-section geometry and material property. However, bone is an inhomogeneous material, *E* and *G* are not constant over femur cross-section. The calculation of the stiffness parameters therefore are conducted by integration:

$$\begin{aligned} K_a &= EA = \int E_i(\rho_i)\,dA \\ K_b &= EI = \int E_i(\rho_i)\; y_i^2\,dA \\ K_s &= GA = \int G_i(\rho_i)\,dA = \frac{K_a}{2\,(1+\upsilon)} \end{aligned} \tag{3.2}$$

Where υ is the poison ration, which is considered to be constant here. ρ_i is the bone mineral density of *ith* pixel or voxel. y_i is the distance of the pixel or voxel to the effective neutral axis, which is substituted with the mid-axis of the image (antero-posterior) in this study for simplicity. The actual neutral axis can be determined by developing an algorithm based on the definition of neutral axis for inhomogeneous cross-section.

Elasticity modulus is related to bone mineral density by mathematical relationships. The accurate determination of such a relationship is of great importance and challenging. Extensive experiments have established that bone elasticity modulus is related to bone mineral density either by linear or by exponential functions [81, 82]:

$$E_i \sim \rho_i \rightarrow E_i = \begin{cases} a\rho_i + b \\ a\rho_i^b \end{cases} \tag{3.3}$$

Hereinafter the term *elasticity-density relationship* will be used for those mathematical relationship between elasticity modulus and bone mineral density. Based on the range of bone mineral density

[81], three representative *elasticity-density relationships* were employed in this study to investigate how different material models affect the 3-D~2-D correlation:

$$\mathrm{E}_i = \begin{cases} 0.573 \cdot \rho_i - 0.0094 \\ 8.92 \cdot \rho_i^{1.83} \\ 2.017 \cdot \rho_i^{2.46} \end{cases} \qquad (\mathrm{E}_i \rightarrow GPa, \rho_i \rightarrow g/cm^3) \qquad (3.4)$$

3.4 Femur Cross-Sectional Properties Derived from QCT Scans

3.4.1 Identification of Three Critical Cross Sections of Femoral Bone from QCT Scans

Quantitative Computed Tomography or "QCT" is a medical imaging technique to evaluate bone mineral density, clinically at the proximal femur or the lumbar spine [83]. The generated volumetric data set contain a wealth of information about bone mineral density, bone mass distribution and geometry. QCT PRO software (Mindways, Texas, USA) can be used to analyze CT volumetric data set. The CTXA-Hip module in QCT Pro can produce DXA-equivalent hip measurements from a CT volumetric data set including areal BMD estimates and bone projection images (CTXA) that are equivalent to those generated by clinical DXA. One sample CTXA is shown in Figure 3.1.

Figure 3.1 A sample CTXA image generated by the QCT PRO software

The Bone Investigational Toolkit included in the QCT PRO software can be employed to analyze the geometry information of bone to estimate biomechanical relevant properties such cross-sectional moment of inertia, section modulus and cross-sectional area. The three critical cross-sections are automatically located in the CTXA image and the cross-sectional images are exported in the format of Digital Imaging and Communications in Medicine (DICOM) shown in Figure 3.2 [84].

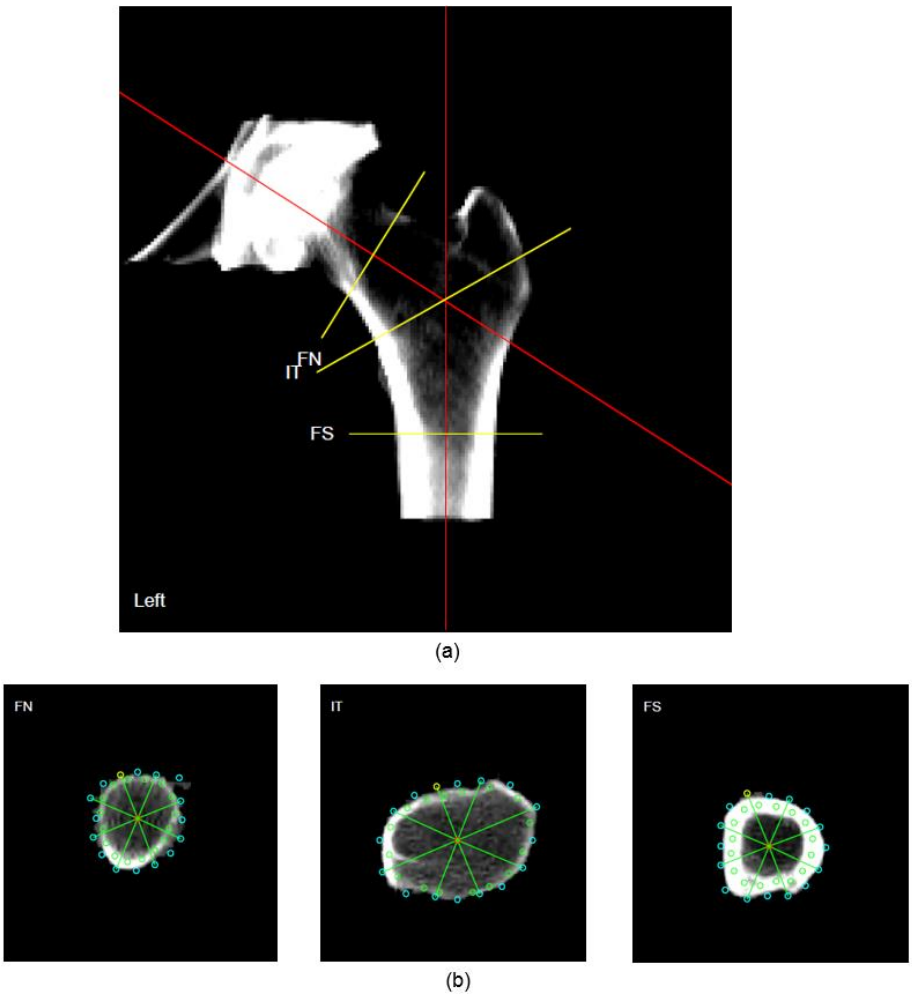

Figure 3.2 QCT Pro-derived information. (a) The three critical cross-sections from CTXA image; (b) BIT-generated three cross-sections

3.4.2 Calculation of Cross-Sectional Stiffness from QCT PRO Image

The cross-section image (DCM format) extracted from QCT PRO was imported into MATLAB using the function "dicomread". The information of the image was then stored in a pixel array with the size of 192x192 in this study. In the pixel array, the coordinates and the pixel value of each pixel can be found using MATLAB. Each of the pixel value describes how bright that pixel is, or the density of bone. Generally, a linear correlation is assumed between pixel value and density [67,

85]. In this study, the volumetric bone mineral density of each pixel corresponding to the pixel value is obtained by the following equation [84]:

$$vBMD(\rho_v) = \frac{FUC \times (\text{p\_value\_CT} - \text{Intercept})}{Slope} (\text{mg}/\text{cm}^3) \tag{3.5}$$

Where

FUC——Field Uniformity Correction,1.073.

p_value_CT—— pixel value in CT image(p_value>0).

Intercept (CT calibration Intercept)—— pixel counts,-1024.

Slope(CT calibration Slope)—— $(mg/cm^3)/count$,1.28.

In order to calculate the stiffness parameters, the first step is to determine the elasticity and shear modulus. Bone is essentially a heterogeneous material. The elasticity and shear modulus vary over a cross-section. As described in Section 3.3.1, three relationships between bone elasticity modulus and bone mineral density were adopted

$$\mathrm{E_i} = \mathrm{E}_i(\rho_i) \tag{3.6}$$

Where the bone elasticity modulus is in GPa , ρ_i is in g/cm^3 .

Due to inhomogeneity of bone density and irregularities of femur cross-section, the stiffness parameters in Equation (3.2) must be calculated by numerical integration. After substituting Equation (3.6) into (3.2), and conducting the integrations in a voxel-by-voxel way, as

shown in Figure 3.3, the axial (*EA*), bending (*EI*) and shearing (*GA*) stiffness of each cross-section , the moment of inertia I, and the section modulus Z are calculated as [86]

$$
\begin{aligned}
&K_{b\_QCT}=EI\_QCT=\int E_i y_i^2 dA=\sum_{i=1}^{N} E_i(\rho_i) y_i^2 dA \\
&K_{a\_QCT}=EA\_QCT=\int E_i dA=\sum_{i=1}^{N} E_i(\rho_i) dA \\
&K_{s\_QCT}=GA\_QCT=\int G_i dA=K_{a\_QCT}/(1+\nu) \\
&I\_QCT=\sum_{i=1}^{N} y_i^2 dA \\
&Z\_QCT=\frac{I\_QCT}{y_{max}}
\end{aligned}
\tag{3.7}
$$

Where E_i represents the modulus of elasticity for *ith* pixel; *dA* is the pixel area; y_i is the distance of each pixel to the mid-axis; y_{max} is the maximum distance to the mid-axis; *N* is the total numbers of the pixels in the bone contour. υ is Poisson ratio, considered as a constant ($\upsilon=0.3$) [87].

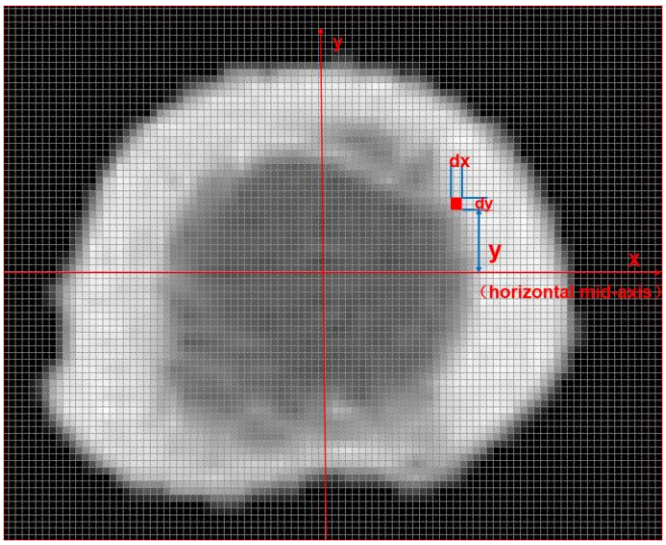

Figure 3.3 The cross section of the image extracted from QCT Pro. *y* is the distance of a single pixel to horizontal mid-axis

3.5 Femur Mechanical Properties Derived from CTXA Images

3.5.1 Data Extraction from CTXA Image

As discussed above, CTXA image is generated through QCT PRO software (Mindways, Texas, USA). A CTXA image is obtained by projecting volumetric bone density in a given direction [88]. If femur cross-section stiffness parameters derived from CTXA are equivalent to those directly derived from QCT, it would suggest that a beam model of femur can be constructed from CTXA (or clinical DXA). The beam model would have wide clinical applications, as DXA is most commonly scanned in clinic.

In order to derive femur cross-sectional mechanical properties from CTXA, the three critical lines in CTXA images corresponding to the three critical cross sections need to be located. Therefore, in-house MATLAB codes were developed to extract the contour of femoral bone. The codes are able to detect femur edge, identify the relevant axes and points, obtain the boundary coordinates, and determine the critical cross sections from CTXA.

The data extraction process is briefly described in Figure 3.4. It consists of extracting contour of femur, finding the FNA (femoral neck axis) and FSA (femoral shaft axis), deciding NFN (narrowest femoral neck), IT (Intertrochanter) cross-section and FS (femoral shaft) cross-section, and locating the FHA (femoral head apex).

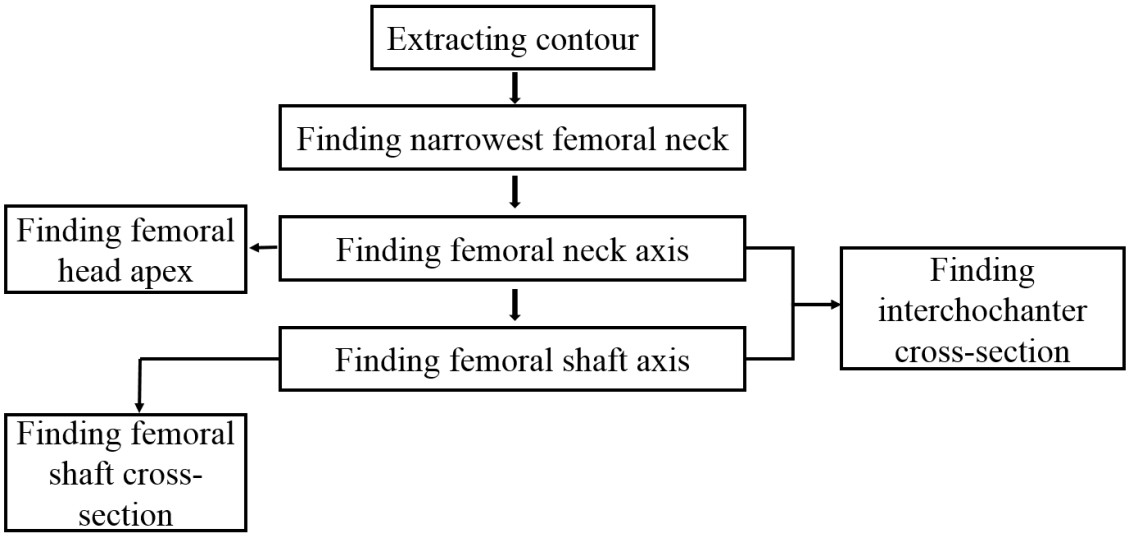

Figure 3.4 Steps for extracting data from CTXA image

The steps for extracting femur contour from CTXA is shown in Figure 3.5. The image was read into MATLAB using 'Dicomread' command. After edge sharpening and dilating, filling interior gaps, and smoothing the object, the outline of the image was then extracted, shown as the white line in Figure 3.6.

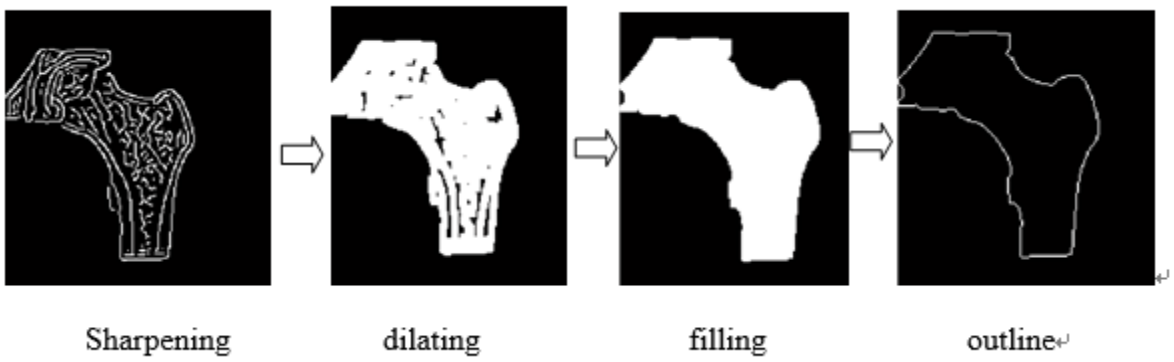

Figure 3.5 Extraction process of the outline of femoral bone

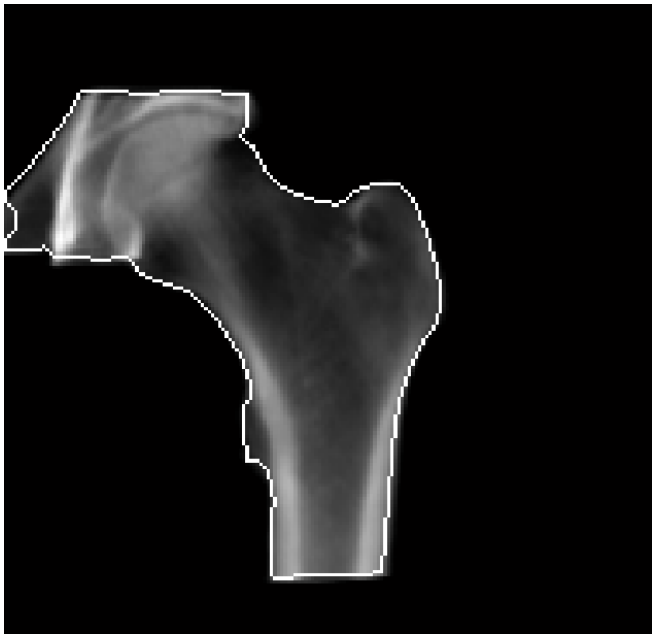

Figure 3.6 Detected contour of femur and part of the pelvis

User's intervention was required to locate the narrowest femoral neck (NFN), femoral shaft (FS) cross-section, and femoral head apex (FHA). The first step was to find the narrowest femoral neck (NFN). Based on the geometry feature of femur, the NFN has the minimum width in the neck region, and the femoral neck axis (FNA) is orthogonal to the NFN and through the mid-point of the NFN [89]. The perpendicular line passing through the mid-point of the shaft cross-sections is the femoral shaft axis (FSA) [90]. The user needs to specify a femoral shaft region (here is the rectangular selection region) including a segment of femoral shaft, and use the mean mid-points of those cross-sections to decide the FSA. Otherwise, the FSA will be very different if only decided by the mid-point of a single shaft cross-section due to the positioning error. Figure 3.7 shows the detected NFN, FNA and the rectangular selection region.

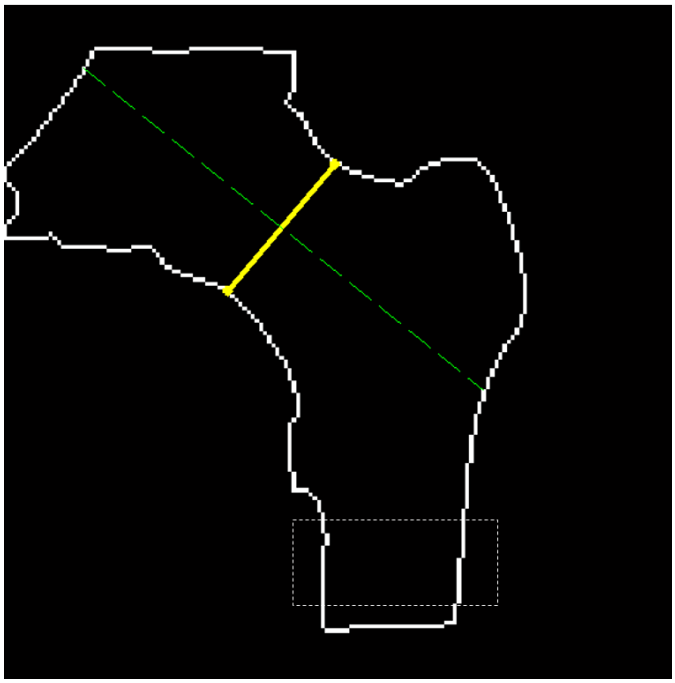

Figure 3.7 The detected NFN, FNA and the rectangular selection region

The IT cross-section line was identified as the line that bisects the femoral neck-shaft axis angle (FNSA) [91]. Also, the FS cross-section line was defined 1.5 times the length of NFN distal to the intersection point of the neck-shaft axes and parallel to the horizontal axis. Finally, the femoral head apex was identified as the smallest pixel value between the femoral head and the pelvis bone around it.

All of the above procedure was implemented using the in-house MATLAB codes. The three critical cross-sections, the femoral head apex, and the femoral neck and shaft axis are shown in Figure 3.8, and the coordinate of the relative parameter was written into an EXCEL table.

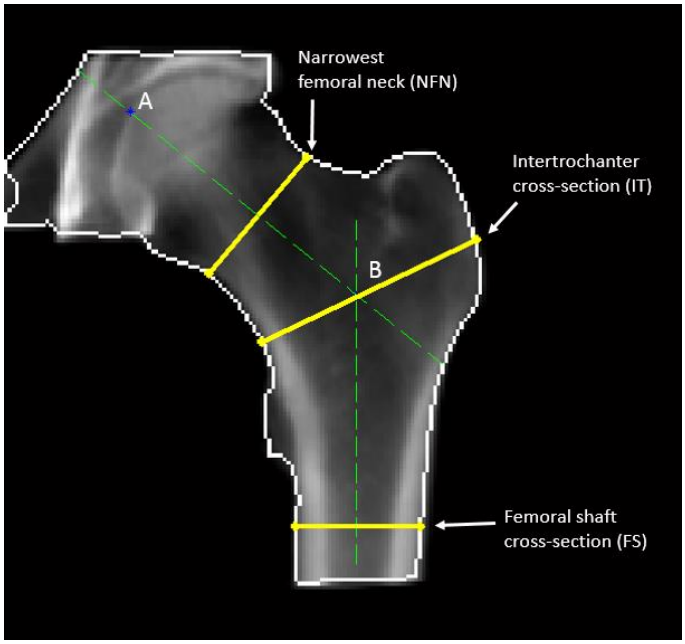

Figure 3.8 The three critical sites of hip: NFN, IT, and FS. A is the femoral head apex, B is the intersection point of femoral neck and shaft axis.

3.5.2 Relation between Pixel Value and aBMD in CTXA Image

The DXA-equivalent two-dimensional CTXA images are projectional images from the QCT 3-D data set. Each pixel intensity in CTXA is the sum of all the bone voxel intensity along the projection lines [88]. Therefore, the three critical cross section lines in CTXA images are the projections of the corresponding cross sections in QCT scans. This process is schematically shown in Figure 3.9 [47, 92]. The projection line of the QCT slice in CTXA is replaced by a rectangle with a width because it can show the density variation along the line. Correspondingly, the bone mineral density in CTXA is transferred to areal BMD from the volumetric BMD in QCT scans as shown in Figure 3.9(c).

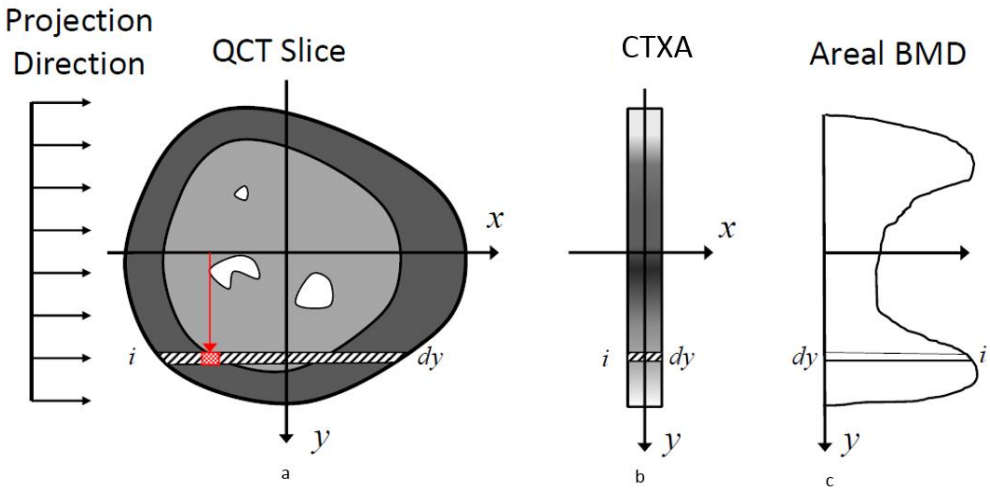

Figure 3.9 Projection from QCT into CTXA. (a) QCT slice (a femur cross-section); (b) the projected cross-section; (c) areal BMD profile [92]

In Section 3.5.1, the coordinate of the three critical cross section line have already been located. By importing the CTXA image into the MATLAB software and using a command 'improfile', the pixel values along the line segments will be obtained. An important step is to derive the relation between pixel value and areal BMD. Generally, the linear relation is assumed as follows:

$$a \cdot p\_value\_CTXA + b = \rho_a \tag{3.8}$$

Where p_value_CTXA represents each pixel value in CTXA image, ρ_a is the corresponding areal BMD.

ave_p_value_CTXA is defined as:

$$ave\_p\_value\_CTXA = \frac{\sum (p\_value\_CTXA) \cdot \mathrm{dA}}{\mathrm{N} \cdot dA} \tag{3.9}$$

Where $\sum p\_value\_CTXA$ is the sum of the pixel value in the ROI area of the femoral neck in the CTXA image, which is a user-defined region based on the reference [91], as shown in Figure 3.10. The blue line is the central line of the ROI, which is the narrowest femoral neck identified in Section 3.5.1. The width of the ROI is 10mm as shown in green region. dA and N are the pixel area and the total pixel numbers in the ROI respectively.

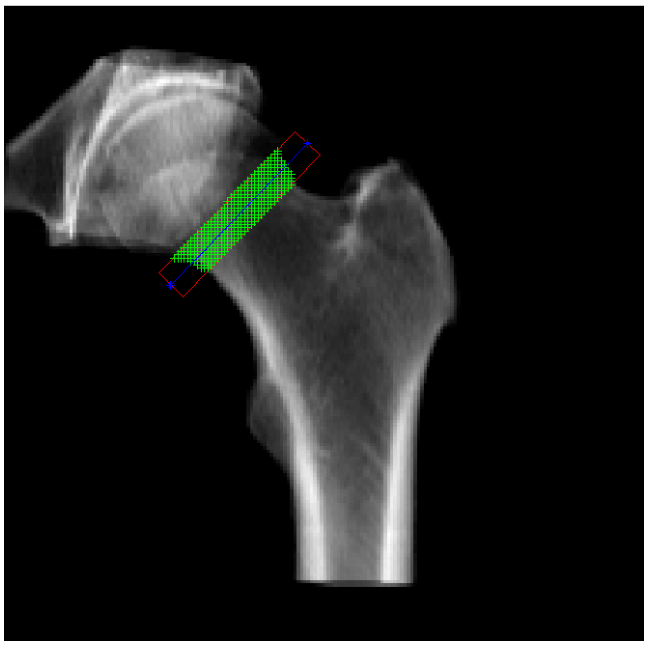

Figure 3.10 ROI region in CTXA.

In this project, using $ave\_p\_value\_CTXA$ as independent variables, ρ_{a_QCT} as dependent variable, regression analysis was performed among different size of sample out of the overall sample respectively, with 5, 10, 15, 20 samples, etc. The corresponding relationships between pixel value and areal BMD were built. ρ_{a_QCT} is the average areal BMD of the ROI area based on QCT PRO report. The error e is defined as the square of the difference between the actual

areal bone mineral density and the estimated bone mineral density. For each equation created by the linear regression analysis, a sum of e was obtained, shown as Equation (3.10).

$$\begin{aligned} e &= (\rho_{a\_estimated} - \rho_{a\_QCT})^2 \\ e' &= \sum e \end{aligned} \tag{3.10}$$

The convergence study was performed using e' to decide the most accurate regression equation. The convergence curve was shown in Figure 3.11. As shown, the third equation had the smallest e' and obtained the convergence, therefore, the third regression equation was chosen to represent the relationship between the pixel value and the areal bone mineral density, as shown in Equation 3.11.

$$\rho_a = 7e-6 \cdot p\_value\_CTXA + 0.6432 \tag{3.11}$$

Where ρ_a is the estimated areal BMD of each pixel in CTXA image, with the unit g/cm^2.

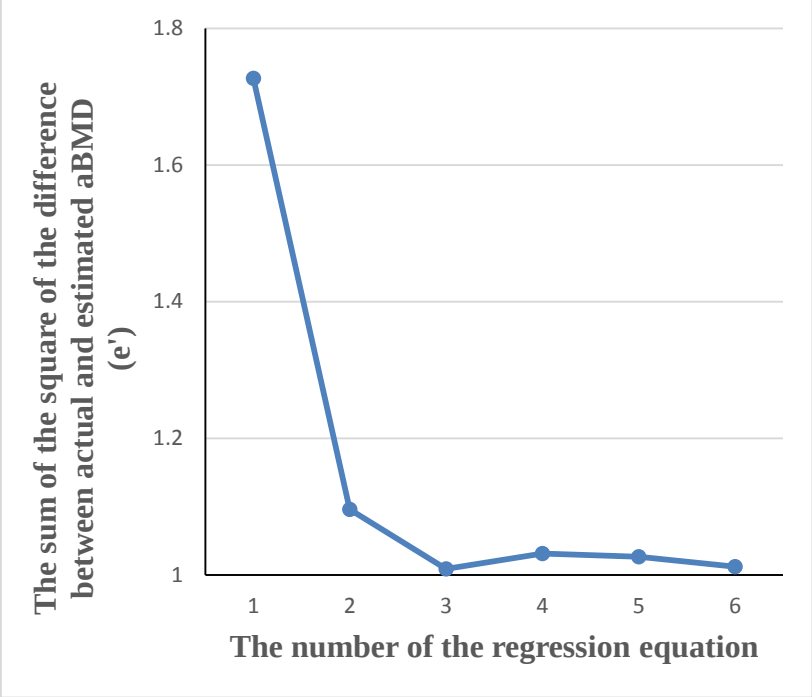

Figure 3.11 The convergence study to decide the most accurate relationship between the pixel value and areal BMD

3.5.3 Correlation Between aBMD in CTXA and vBMD in QCT

After transferring the pixel value into the areal BMD in CTXA image based on the Equation (3.11), the next step is to develop a conversion formula between areal BMD and volumetric BMD in order to reduce the difference in stiffness derived from QCT and CTXA images, since the bone mineral density is volumetric BMD in QCT image and areal BMD in CTXA image. With the same described in Section 3.5.2, correlation and regression analysis were conducted between aBMD and vBMD based on QCT PRO data, and the convergence study was performed to decide the most accurate relationship.

Totally, there were five groups of paired aBMD and vBMD provided in QCT Pro reports, which are user-defined neck, femoral neck, trochanter, intertrochanter and total hip aBMD and vBMD, for 97 subjects. Different number of samples, namely 15, 20, 25, 30, etc., were randomly selected from the five groups of paired aBMD and vBMD, to produce sample datasets. Then, linear regression analysis was conducted in each dataset to obtain an equation. In the regression equation, vBMD is calculated from aBMD. As described in Section 3.5.2, the square of the difference between estimated vBMD and the measured vBMD was calculated as *e*, then the convergence study was conducted using *e'*, as shown in Figure 3.12 .

$$\begin{aligned} e &= (\rho_{v\_estimated} - \rho_{v\_QCT})^2 \\ e' &= \sum e \end{aligned} \tag{3.12}$$

Based on the convergence curve, the fourth regression equation was more accurate, which was obtained by the dataset of 150 samples consisting of 30 samples from the five groups. The most accurate regression formula is

$$y = 0.29348 \cdot x + 0.055042 \tag{3.13}$$

Where x represent the aBMD (g/cm^2), y is the vBMD (g/cm^3). The correlation between aBMD and vBMD was shown in Figure 3.13. The correlation coefficient is

$$R = 0.87475 (\mathrm{P} < 0.001) .$$

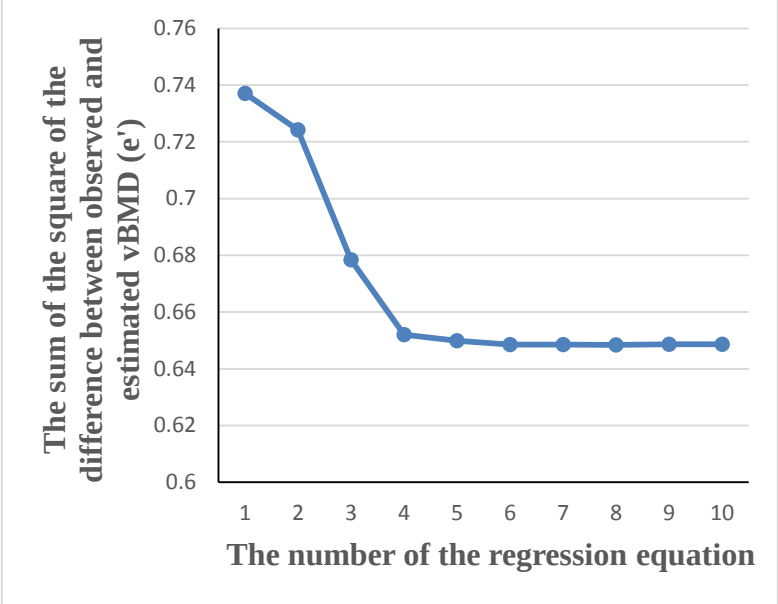

Figure 3.12 The convergence study to decide the most accuracy relationship between aBMD and vBMD

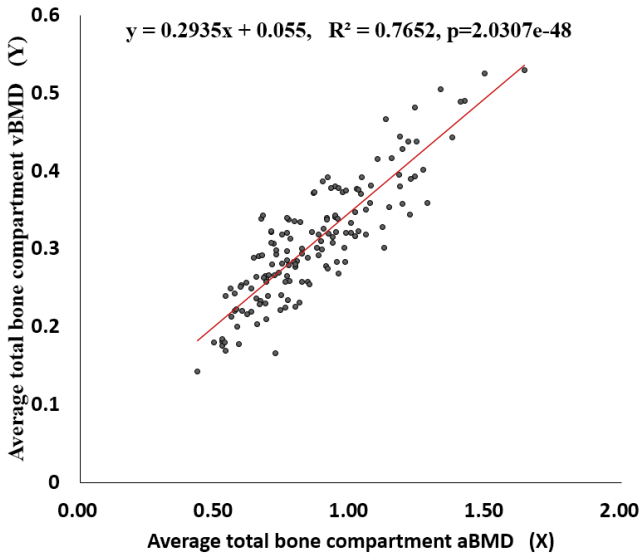

Figure 3.13 Correlation between aBMD and vBMD

For the cases that were not included in the sample datasets, vBMD were calculated from aBMD using the regression formula, at respectively, user-defined neck (UDF), femoral neck (FN), trochanter (T), intertrochanter (IT) and total hip (TH). The correlation coefficients between the calculated vBMD and the vBMD directly measured by QCT Pro are listed in Table 3.1. The Bland-Altman plots are shown in Figure 3.14.

From Table 3.1, it can be seen that the vBMD calculated from the regression formula is strongly correlated with the vBMD measured by QCT PRO. In Figure 3.14, the Bland-Altman plots show that the agreement level is acceptable. Therefore, the conversion formula was used to convert aBMD into vBMD.

Table 3.1 Correlation coefficient between estimated and measured vBMD at the five sites

	UDN	**FN**	**T**	**IT**	**TH**
r	0.7767	0.8253	0.9178	0.8614	0.8813
p	8.7997e-21	2.6262e-25	6.8739e-40	1.0733e-29	1.0866e-32

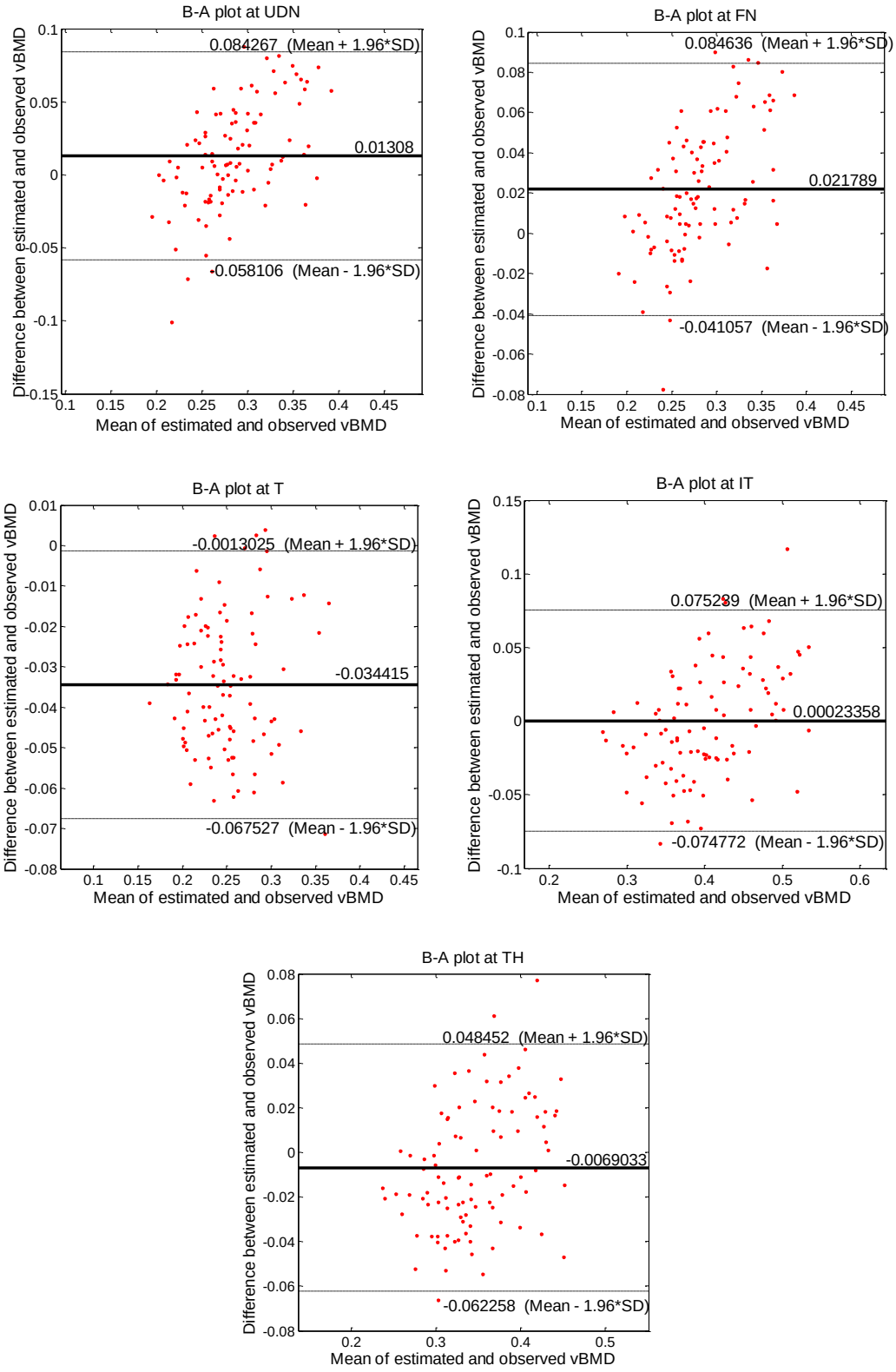

Figure 3.14 Bland-Altman plot of measured vBMD and calculated vBMD using the regression formula.

3.5.4 Calculation Cross-Sectional Stiffness from CTXA Image

The three critical cross-sections where hip fractures most often occurred are indicated by the three yellow lines in CTXA shown in Figure 3.8. As described in Section 3.5.2, the coordinates and the pixel values of the line can be obtained by MATLAB codes, then the areal bone mineral density of each pixel on the line can be calculated based on Equation (3.11). Using the regression Equation (3.13), vBMD of each pixel on the line can be obtained. As described in Section 3.4.2, the elasticity-density relation was adopted as the empirical Function (3.6), and stiffness parameters was calculated by integration along the line. In a pixel-by-pixel way along the cross section line, the integration was carried out, and the axial (EA), bending (EI) and shearing (GA) stiffness of each cross section line in CTXA are calculated. The calculation method is described in Section 3.4.2.

$$
\begin{aligned}
\mathrm{K}_{b\_CTXA} &= \mathrm{EI\_CTXA} = \int \mathrm{E}_i \mathrm{y}_i^2 \mathrm{dA} = \sum_{i=1}^{N} E_i(\rho_i) y_{i\_CTXA}^2 dA \\
\mathrm{K}_{\mathrm{a\_CTXA}} &= \mathrm{EA\_CTXA} = \int \mathrm{E}_i \mathrm{dA} = \sum_{i=1}^{N} E_i(\rho_i) d\mathrm{A} \\
\mathrm{K}_{\mathrm{s\_CTXA}} &= \mathrm{GA\_CTXA} = \int G_i dA = {}^{\mathrm{K}_{\mathrm{a\_CTXA}}}\!/_{1+\nu}
\end{aligned}
\tag{3.14}
$$

Where ρ_i, the volumetric BMD, is regressed from areal BMD in the cross-section image of CTXA, and has the unit of g / cm^3; N is the total numbers of the pixels along the cross-sectional line in CTXA images; y_{i_CTXA} is the distance of the *ith* pixel to the mid-point of the cross-sectional line in CTXA images; dA is the product of the thickness of the *ith* pixel in the profile and pixel spacing along the profile line. The thickness of the *ith* pixel is calculated by divided the vBMD by aBMD.

Chapter 4

Assessment of Hip Fracture Risk Using CTXA-based Beam Model

4.1 Beam Model Constructed from CTXA

Beam model used in this project treats the proximal femur as two straight beams connected at the intertrochanter, as shown in Figure 4.1. Angle θ is the neck-shaft axis angle, and the intertrochanteric cross-section bisects this angle. Point *h* and *k* represent the femoral head apex and distal femur end, respectively, and point *o* is the intersection of the femoral neck and shaft axis. The angle θ and the coordinates of these points and the three critical cross-sections femoral neck (FN), intertrochanter (IT) and femoral shaft (FS) are located by MATLAB codes. The procedure for extracting data from CTXA image is described in Section 3.5. Based on these information, the geometry properties of the beam can be extracted. The length $\overline{ok}$, i.e. the femoral shaft length (FSL), is estimated from the patient's height *H* [93],

$$\overline{ok}(\text{FSL}) = \frac{1}{5}H \tag{4.1}$$

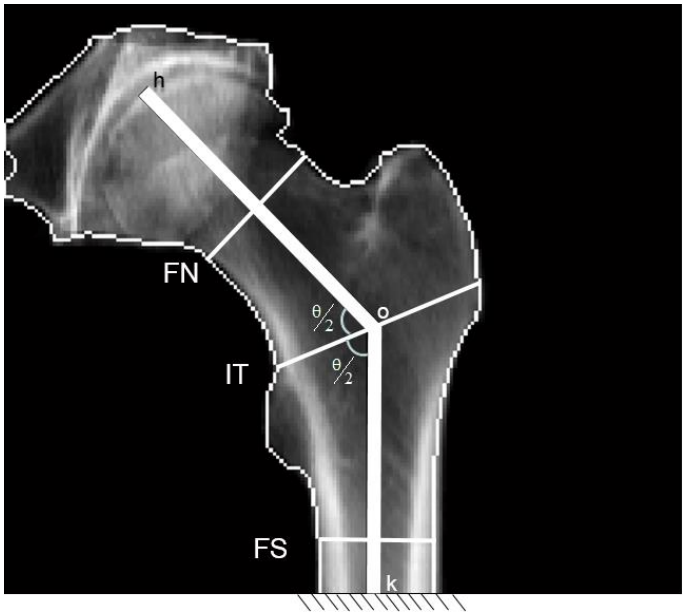

Figure 4.1 Beam model constructed from CTXA image

4.2 Loading Conditions

There are different loading configurations that can be applied to the two-dimensional beam model. Two of them represent the real life conditions and they commonly used in hip fracture studies: (1) one-legged stance and (2) sideways fall. The one-legged stance condition is often used for comparison among different studies [75, 76]. Sideways fall has been identified as the most critical condition, especially for older people, to develop hip fracture [94, 95]. Therefore, these two loading conditions will be considered in the following studies, and the forces (including moment) diagrams are determined based on static equilibrium.

4.2.1 One-Legged Stance Configuration

To simulate one-legged stance loading condition, the proximal femur is loaded on the femoral head apex and completely constrained at its distal end, as shown in Figure 4.2. The load on the femoral head is calculated as 2.5 times body weight [96, 97] of the subject in Newton (N), and the direction of the load is assumed parallel to femoral shaft [40, 98]. The load can be projected into axial and normal component relative to the femoral neck axis.

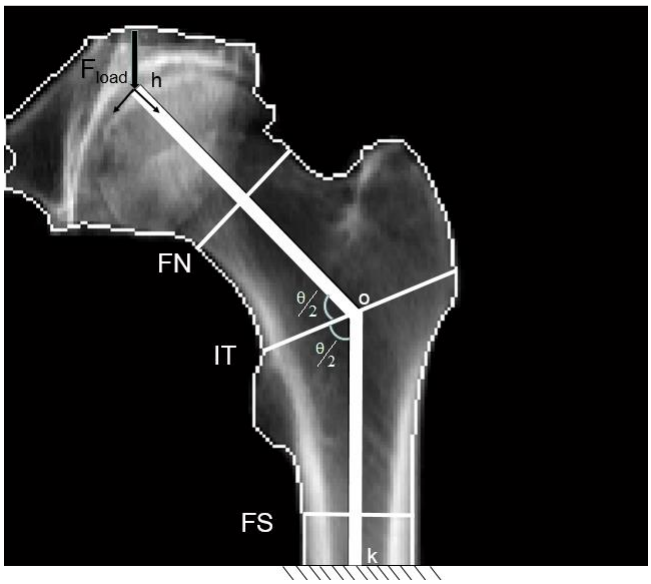

Figure 4.2 The loading condition of femoral beam model in a one-legged stance

Based on the principles of statics, the internal forces at the three critical cross-sections, i.e. FN, IT and FS, are shown in Figure 4.3.

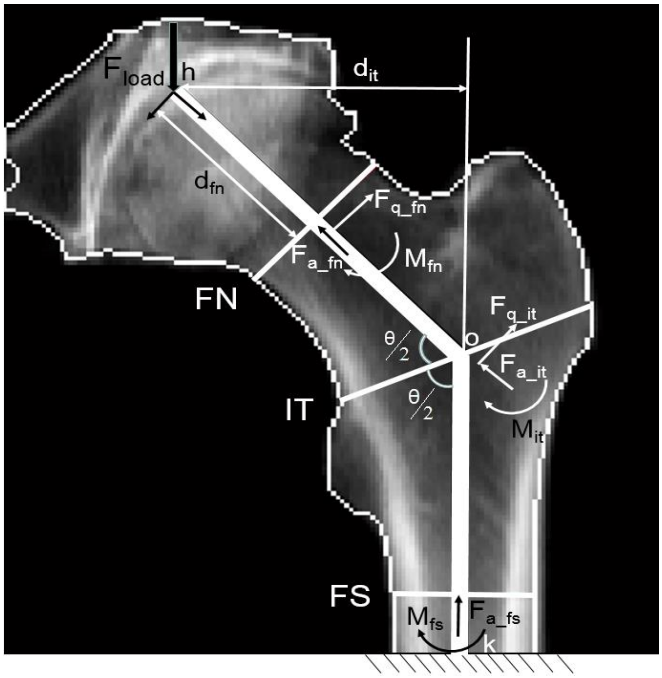

Figure 4.3 The force diagrams at the three critical cross-sections

At cross-section FN, the axial force F_{a_fn}, shear force F_{q_fn} and bending moment M_{fn} are calculated as

$$\begin{cases} F_{a\_fn} = F_{load}\cos(180-\theta) \\ F_{\mathrm{q\_fn}} = F_{load}\sin(180-\theta) \\ \mathrm{M_{fn}} = F_{load}\sin(180-\theta)\cdot d_{fn} \end{cases} \tag{4.2}$$

Cross-section IT is the intersection point of the neck and the shaft axis, therefore, both axes are considered for calculation the forces. That is, IT cross-section is either considered as the cross-section of femoral neck axis, or as the cross-section of femoral shaft axis to calculate the forces. However, the total strain energy induced by the axial, bending and shear force does not show too much difference (calculated in the later section). Therefore only femoral neck axis is used to show the forces on IT cross-section:

$$\begin{cases} F_{a\_it} = F_{load}\cos(180-\theta) \\ F_{q\_it} = F_{load}\sin(180-\theta) \\ \mathrm{M}_{it} = F_{load}\cdot d_{it} \\ d_{it} = \overline{ho}\cdot\sin(180-\theta) \end{cases} \tag{4.3}$$

For cross-section FS,

$$\begin{cases} F_{a\_fs} = F_{load} \\ F_{q\_fs} = 0 \\ \mathrm{M}_{fs} = F_{load}\cdot d_{it} \\ d_{it} = \overline{ho}\cdot\sin(180-\theta) \end{cases} \tag{4.4}$$

As mentioned above,

$$F_{load} = 2.5\cdot W \tag{4.5}$$

Where W is the body weight of the subject.

4.2.2 Sideways Fall

The dominant cause leading to hip fracture is sideways fall, especially for elderly people suffering from osteoporosis. A set of static forces are used to simulate the peak impact force in sideways fall in the real world. Figure 4.4 shows the forces experienced by the femur in sideways fall, and the free body diagram is shown in Figure 4.5. Under this loading condition, the impact force is assumed perpendicular to the shaft axis and at the intersection point of the femoral neck-shaft axis. Two reaction forces are produced respectively at the femoral head apex and at femur distal end with a distance of 0.2 times patient's body height, they are shown as F_h and F_k respectively [76]. This distance is femoral shaft length (FSL), shown in Figure 4.4.

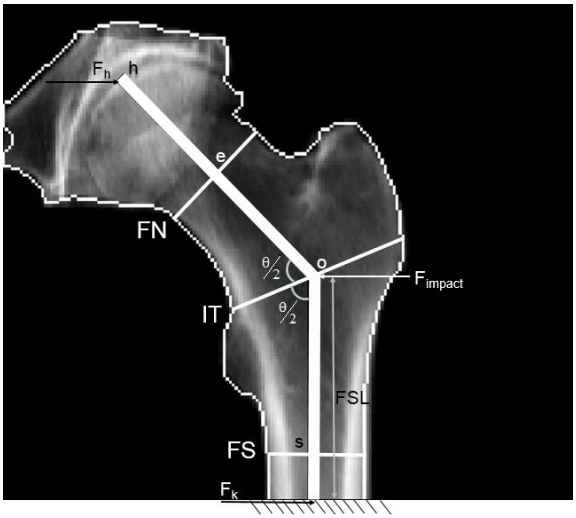

Figure 4.4 Loading/constraint profile of the femur beam model

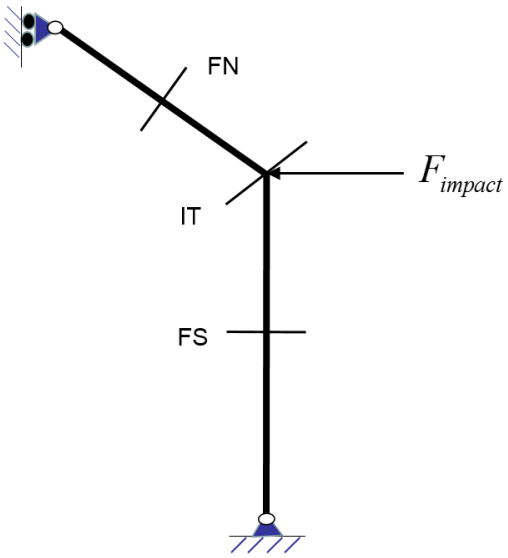

Figure 4.5 Free body diagram simulating sideways fall

According to Robinovitch et al. [99], the impact force and FSL can be estimated using the following empirical functions

$$\begin{cases} F_{impact} = 8.25 \cdot W \cdot \left(\frac{H}{170}\right)^{\frac{1}{2}} \\ FSL = 0.2 \cdot H \end{cases} \tag{4.6}$$

Where H and W represent respectively body height in centimeter (cm) and body weight in Newton (N) of the concerned subject.

The internal forces at the three critical cross-sections are shown in Figure 4.6. Based on static force equilibrium, force $\mathrm{F_h}$ and F_k can be calculated as

$$\begin{cases} F_{impact} \cdot FSL = F_h \cdot (\mathrm{FSL} + \overline{\mathrm{ho}} \cdot \sin(\theta - 90)) \\ F_{impact} - F_h = F_k \end{cases} \Rightarrow F_h, F_k \tag{4.7}$$

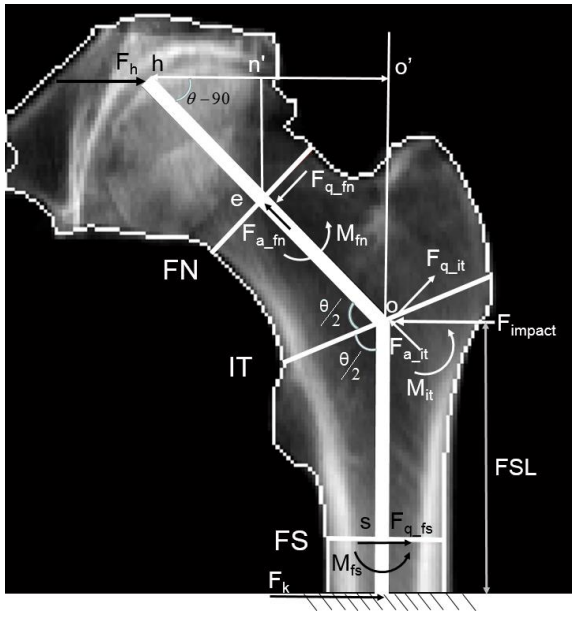

Figure 4.6 The internal forces at the three cross-sections in sideways fall

After calculating force F_{impact}, F_h and F_k, the internal forces at the three critical cross sections can be determined.

For femoral neck (FN),

$$\begin{cases} M_{fn} = F_h \cdot \overline{he} \cdot \sin(\theta - 90) \\ F_{a\_fn} = F_h \cdot \cos(\theta - 90) \\ F_{q\_fn} = F_h \cdot \sin(\theta - 90) \end{cases} \tag{4.8}$$

Similarly, for cross-section IT, only femoral neck axis is used to show the forces on IT cross-section

$$\begin{cases} M_{it} = F_h \cdot \overline{ho} \cdot \sin(\theta - 90) \\ F_{a\_\mathrm{it}} = (F_{impact} - F_h) \cdot \sin(180 - \theta) \\ F_{q\_\mathrm{it}} = (F_{impact} - F_h) \cdot \cos(180 - \theta) \end{cases} \tag{4.9}$$

For cross-section FS,

$$\begin{cases} M_{fs} = F_{impact} \cdot \overline{os} - F_h \cdot (\overline{os} + \overline{ho} \cdot \sin(\theta - 90)) \\ F_{a\_\mathrm{fs}} = 0 \\ F_{q\_\mathrm{fs}} = F_{impact} - F_h \end{cases} \tag{4.10}$$

4.3 Fracture Risk Index

4.3.1 Cross-Sectional Strain Energy Failure Criterion

For the assessment of hip fracture risk, there are different failure criteria, for example strain-based criteria [53, 100], stress-based criterion [101], energy-based criterion [102], etc. However, stress- and strain-based failure criteria are suitable for either ductile or brittle material, they may not be

able to accurately describe bone failure because cortical bone is classified to be brittle and cancellous bone is ductile [103]. Therefore, both of distortion energy and volume change energy should be considered in the failure analysis of hip fracture risk. The energy stored in a material body caused by deformation is called strain energy. The total strain energy is the combination of distortion energy and volume change energy. Therefore, the total strain energy is theoretically a better criterion to evaluate bone failure due to its ability to accommodate both ductile and brittle failure. In this study, hip fracture risk index (FRI) over the three critical cross section is defined based on the strain energy criterion.

4.3.2 Strain Energy at the Three Critical Cross-Sections

Strain energy is the potential energy produced by stress and deformation of material. Generally, the total strain energy of an engineering beam subjected to axial, bending, shear and torsional forces is the sum of the strain energy due to axial, bending, shear and torsional deformation. However, as discussed before, for the femur beam model constructed from two-dimensional CTXA image, torsion is not considered. Therefore, in this study, only the strain energy of axial, bending and shear deformation are considered.

According to material mechanics, the strain energy at an arbitrary cross-section of femur induced by the axial, bending and shear force are calculated respectively as,

$$\begin{cases} U_a = \dfrac{\mathrm{F}_a^2}{2(EA)} \\ U_b = \dfrac{\mathrm{M}_b^2}{2(EI)} \\ U_s = \dfrac{\mathrm{F}_q^2}{2(GA)} \end{cases} \tag{4.11}$$

Where U_a, U_b and U_s are the strain energy corresponding to the axial force F_a, bending moment M_b and shear force F_s. EA, EI and GA are the cross-sectional stiffness of the beam, which have been described in Section 3.5.4. Therefore, the total strain energy on the cross-section is

$$U = U_a + U_b + U_s \tag{4.12}$$

The formulas for calculating the axial, bending and shear forces under the two loading conditions on the three critical cross-sections have been introduced respectively in Section 4.2.1 and 4.2.2, and the cross-sectional stiffness are obtained in Section 3.5.4, the total strain energy on the three critical cross-sections in the beam model can be computed based on Equations (4.11) and (4.12) using in-house MATLAB codes.

4.3.3 The Yield Strain Energy of the Three Critical Cross-Sections

For a beam model, the allowable strain energy over a cross-section at the yielding point is given by

$$U_Y = \int_A \frac{1}{2} \cdot \sigma_Y^T \cdot \varepsilon_Y dA = \int_A \frac{1}{2E} \cdot \sigma_Y^2 dA \tag{4.13}$$

Where σ_Y and ε_Y are respectively the yield stress and yield strain at a point over the cross-section. Here the yield stress was chosen instead of ultimate stress because use of ultimate stress for bone

evaluation is too risky. However the yield stress is more conservative for the bone since bone was treated as brittle material. For a femur cross-section projected as a CTXA image, the integration can be conducted in a pixel-by-pixel way as

$$U_Y = \sum_{i=1}^{N} \frac{1}{2E} \cdot \sigma_{Yi}^2 dA \tag{4.14}$$

Where N is the number of pixels along the cross-section line in CTXA image, σ_{Yi} is the yield stress of the *ith* pixel. According to Keller et al [104] and the previous work in our team [92], bone yield stress is correlated to volumetric bone mineral density (g/cm^3) by empirical function,

$$\sigma_{Yi} = 116 \times \rho_{vi}^{2.03} MPa \tag{4.15}$$

ρ_{vi} is the volumetric BMD at the *ith* pixel .

4.3.4 Hip Fracture Risk Index at the Three Critical Cross-Sections

Hip fracture risk index (HFRI) at the three critical cross-sections, including the femoral neck (FN), the intertrochanter (IT), and the femoral shaft (FS), is defined as the ratio of the strain energy caused by the applied forces to the yield strain energy of the femur at the concerned cross-section.

$$\eta_{hfri} = \frac{U}{U_Y} \tag{4.16}$$

Where η_{hfri} is the fracture risk index at one of the three critical cross-sections of the femur. U and U_Y are respectively the strain energy induced by the applied forces and yield strain energy over the cross-section, they are obtained in Equation (4.12) and (4.14).

Chapter 5

Results and Discussion

All of the results obtained in this study are reported in this chapter. Section 5.1 introduces the cases enrolled in this study. Section 5.2 represents the relationships between bone mineral density and elasticity modulus, and comparison of CTXA- and QCT- derived cross sectional stiffness of femur. Section 5.3 reports the correlation analysis results, which will help establish the equivalence between DXA- and QCT- derived cross-sectional stiffness. Section 5.4 presents the results of discriminating PPI users from non-PPI users, by CTXA-based cross-sectional stiffness, bone mineral density, and hip fracture risk respectively.

5.1 Enrollments of Cases

Total of 92 clinical cases were enrolled in this study. The information including QCT image, height, and body weight was obtained from the Winnipeg Science Health Center in an anonymous way under a human research ethics approval. The statistical information is listed in Table 5.1. The heights and body weights range from 124.5-187 centimeters and 55.1-170.6 kilograms, respectively. CTXA images were derived from QCT images through QCT PRO software

(Mindways, Texas, USA) for each case. The correlation between CTXA- and QCT-derived cross-sectional stiffness was investigated. A CTXA-based beam model was constructed for each subject; loading and boundary conditions simulating sideways fall and single-leg stance were applied to each beam model; FRIs were calculated at the three critical cross-sections of femur for each subject.

Table 5.1 Statistics information of the 92 clinical cases

	Height (cm)	Body weight (kg)
Range	124.5-187	55.1-170.6
Average	168.76	84.54

5.2 Relationships between BMD and Elasticity Modulus

As described in the previous section, three elasticity-density relationships were investigated in this study. After substituting Equation (3.4), the three elasticity-density relationships, into the calculation of the cross-sectional stiffness, the corresponding correlation coefficient between CTXA-derived stiffness and QCT-derived stiffness at the three critical cross-sections are listed in Table 5.2. As can be seen from the table, the general trend is the correlations between CTXA- and QCT- derived stiffness are getting worse with higher power exponent. There is some different at FS (not follow the same trend), probably due to that the cross-sections in CTXA and in QCT were mismatched. The linear equation produced the highest correlations. However, for all the elasticity-density relationships, the results in Table 5.2 show that CTXA- and QCT- derived stiffness are highly correlated.

According to extensive experimental studies [81, 87], bone elasticity modulus is correlated to bone density, mostly by exponential relationship. Therefore, in the following study, we only showed the results of the exponential relationship with the lowest exponent, which is

$$E = 8.92 \cdot \rho^{1.83} \tag{5.1}$$

Where E is the elasticity modulus (Gpa), ρ is the volumetric bone mineral density (g/cm^3).

Table 5.2 Correlations between CTXA and QCT derived stiffness at the three critical cross-sections based on different elasticity-density relationships. E is the elasticity modulus (Gpa), ρ is the volumetric bone mineral density (g/cm^3)

Cross-section	**CTXA- derived stiffness**	**QCT- derived stiffness**	$E = 0.573 \cdot \rho - 0.0094$		$E = 8.92 \cdot \rho^{1.83}$		$E = 2.017 \cdot \rho^{2.46}$	
			r	**p**	**r**	**p**	**r**	**p**
FN	EI	EI	0.95038	1.13E-34	0.93338	1.24E-30	0.91161	8.63E-27
	EA	EA	0.79377	1.13E-15	0.70997	1.72E-11	0.64258	4.56E-09
IT	EI	EI	0.87537	3.40E-22	0.87443	4.28E-22	0.86208	7.39E-21
	EA	EA	0.83061	3.50E-18	0.80879	1.24E-16	0.76817	3.28E-14
FS	EI	EI	0.55149	1.32E-06	0.61212	3.74E-08	0.63592	7.37E-09
	EA	EA	0.52985	4.00E-06	0.55771	9.44E-07	0.53212	3.59E-06

5.3 Equivalence between QCT- and CTXA- Derived Cross-Sectional Mechanical Properties

5.3.1 Validation of QCT-derived Cross-sectional Mechanical Properties

Table 5.3 shows the correlation coefficient between femoral-neck mechanical properties derived by in-house MATLAB codes and by QCT Pro software from QCT scan. In Table 5.3, EIx, Ix, Zx, and EIy, Iy, Zy are the bending stiffness, moment inertia, and section modulus in x direction and y direction accordingly, calculated by in-house MATLAB codes in Section 3.4.2."CSMI_inplane" and "CSMI_outplane" are the cross section moment inertia with respect to *x* direction and *y* direction, respectively; "CSA" is cross section area; "SM" represents the section modulus. They are obtained from QCT Pro database. According to Beck et al [40, 76], cross section moment inetia (CSMI), cross section area (CSA) and section modulus (SM) are calculated as

$$\text{CSMI}=\frac{\Delta}{\rho_b}\sum_{i=1}^{N} y_{i\_c}^2\rho_a$$

$$\text{CSA}=\frac{\Delta}{\rho_b}\sum_{i=1}^{N} \rho_a \tag{5.2}$$

$$SM = CSMI / y_{\max\_c}$$

Where Δ is the pixel width along the profile line and ρ_b is the fully mineralized bone density considered as a constant. ρ_a is the pixel bone mass（areal bone density) in g/cm^2 and y_{i_c} is the distance of the *i-th* pixel to the centroid of the bone mass distribution in the profile. $y_{\max\_c}$ is the maximum distance to the centroid.

Table 5.3 Correlation coefficients r (p-value) between femoral-neck stiffness derived by in-house codes and QCT-Pro software from QCT scan

Cross-section	In-house developed	QCT-PRO developed	Correlations	
			r	p
FN	EIx	CSMI_inplane	0.88740	1.53E-23
	EIy	CSMI_outplane	0.88482	3.06E-23
	EA	CSA	0.81373	5.80E-17
	Ix	CSMI_inplane	0.88758	1.46E-23
	Iy	CSMI_outplane	0.86314	5.86E-21
	Zx	SM_inplane	0.86310	5.83E-21
	Zy	SM_outplane	0.86665	2.66E-21

As we can see, mechanical properties developed by in-house MATLAB codes are highly associated with those obtained by QCT-Pro software ($r=0.81$-0.88, $p<0.001$), which suggests that the proposed algorithm to calculate cross-sectional stiffness is reasonably accurate and reliable.

5.3.2 Correlation between QCT- and CTXA-derived Cross-sectional Mechanical Properties

Correlations between CTXA- and QCT- derived mechanical properties of femur are presented in this section. Figure 5. 1 (a-d) shows the correlation between CTXA- and QCT-derived cross-sectional parameters. Figure 5. 1 only lists the cross-sectional parameters at femoral neck, not including the other two critical cross-sections, i.e., interchochanter and femoral shaft because they have the same trend. The overall pattern of the points are not in a perfect straight line, but the linear trend (upward) is clearly shown in each figure. The best fit is shown in red line in each figure.

Take Figure 5.1 (a) as an example, the points are tightly clustered around the underlying form, and the trend is upward. Therefore, QCT-derived and CTXA-derived bending stiffness at femoral neck have a strong positive correlation. The other three figure show similar pattern. Therefore, CTXA- and QCT-derived cross-sectional parameters are strongly and positively correlated. It is worth of mentioning that the shear stiffness has the same trend-line as that of axial stiffness, because there is a linear relationship between elasticity and shear modulus if the Poisson's ration is a constant. In this study, Poisson's ration is assumed as 0.3.

Table 5.4 shows the correlation coefficients at the three critical cross-sections between QCT and CTXA derived cross-sectional properties. As expected, CTXA- and QCT-derived mechanical parameters at the three critical cross-sections are highly correlated; and there is a strong correlation, generally, between each pair based on the correlation coefficient ($r=0.4141$-0.9338, $p<0.001$, as shown in Table 5.4). As can be seen, the correlation coefficients at different anatomic site, namely FN, IT and FS, are quite different. The correlation is highest at FN, and lowest at FS. The reason may come from the elasticity-density relationship. Based on the literature [105], the relationship between elastic modulus and density depends on anatomic site, which means there is no universally accurate relationship for the whole femur. In this study, the elasticity-density relationship was established by power-law regressions for four sites together ("pooled"), including femoral neck [105]. This partially explains why the correlation coefficients at FN are highest. Also, the empirical function employed here is established based on the extensive experiments on cancellous bone [105]. However, we used this function for the whole cross-section without separating the cortical bone and cancellous bone. Obviously, the cortical bone accounts for a large proportion at FS. This may explain why the correlation coefficients at FS are lowest. Therefore, if

the elasticity-density relationship is used in the corresponding site and is separated for cancellous bone and cortical bone in the future study, the correlations are expected higher.

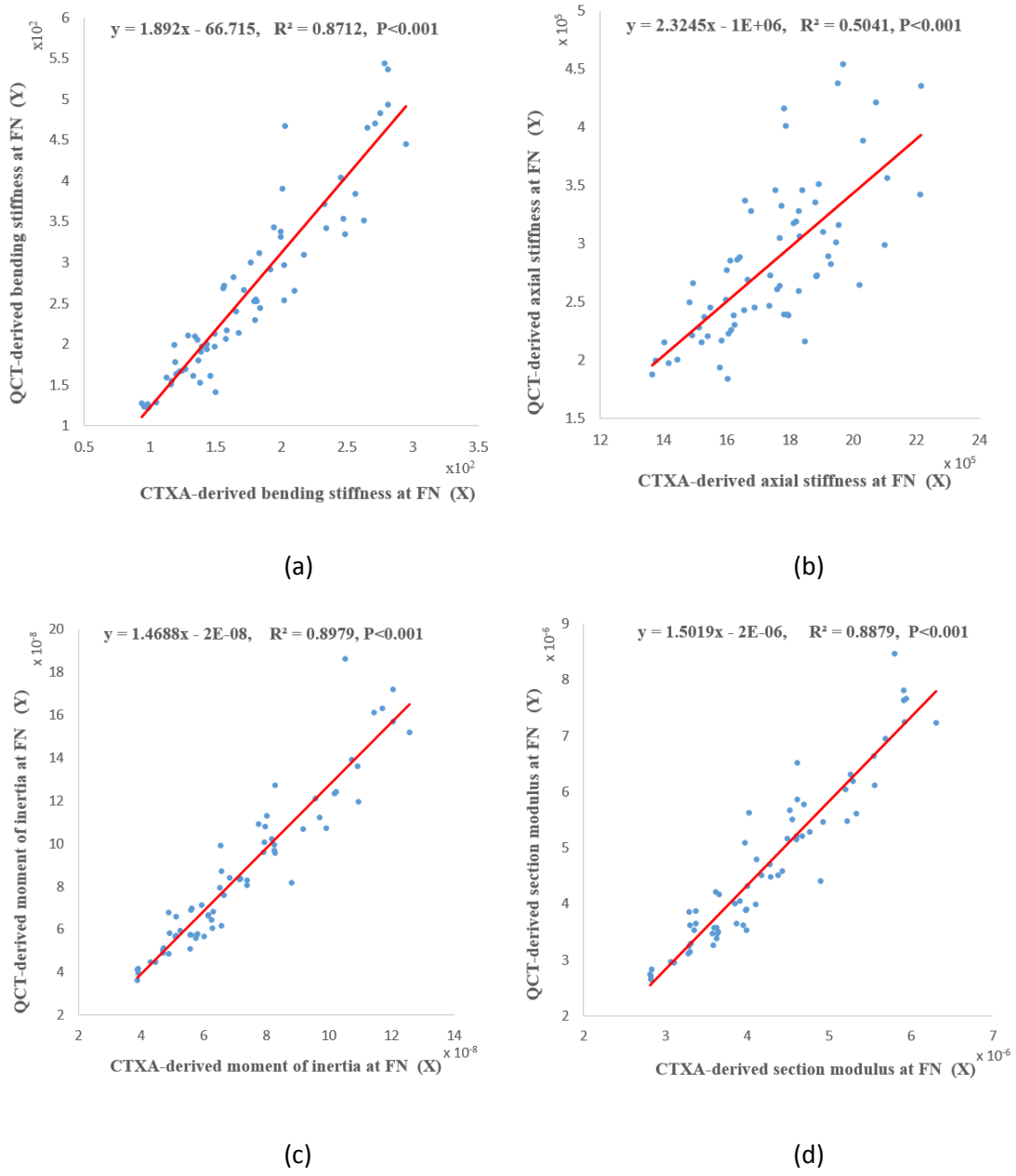

Figure 5.1 Correlations between CTXA- and QCT-derived stiffness at femoral neck (FN). (a) Bending stiffness; (b) Axial stiffness; (c) Moment of inertia; (d) Sectional modulus.

Table 5.4 Correlation coefficients r (p value) between CTXA- and QCT-derived mechanical properties at the three critical cross-sections with elasticity-density relationship: $E = 8.92 \cdot \rho^{1.83}$

Cross-section	CTXA- derived stiffness	QCT- derived stiffness	Correlations	
			r	p-value
FN	EI_2-D	EI_3-D	0.93338	1.24E-30
	EA_2-D	EA_3-D	0.70997	1.72E-11
	I_2-D	I_3-D	0.94756	6.50E-34
	Z_2-D	Z_3-D	0.94229	1.34E-32
IT	EI_2-D	EI_3-D	0.87443	4.28E-22
	EA_2-D	EA_3-D	0.80879	1.24E-16
	I_2-D	I_3-D	0.85401	4.11E-20
	Z_2-D	Z_3-D	0.81535	4.48E-17
FS	EI_2-D	EI_3-D	0.61220	3.74E-08
	EA_2-D	EA_3-D	0.55771	9.44E-07
	I_2-D	I_3-D	0.44756	0.000146
	Z_2-D	Z_3-D	0.41410	0.000494

Another issue is that the correlation coefficients in this study are not as high as expected like that (r=0.93-0.96) produced in our previous published paper [92]. One of the main reasons is that the cross-section image used in the stiffness calculation in CTXA may be not the exactly same with that used in QCT. Although the algorithm in locating the cross-section is the same in CTXA and QCT images, the errors may come from all aspects, such as the difference of the codes used to find the interested cross-sections in CTXA and QCT, different user operations of QCT PRO, and image quality etc. However, in the published paper [92], we use the exactly same cross-section

to produce the two data to calculate the correlation coefficients, which are much higher. Therefore, in the future, if the same cross-section in CTXA and QCT images are used, the correlation coefficients between CTXA- and QCT-derived stiffness will be improved.

Figure 5. 2 shows Bland-Altman plots that demonstrate the comparability between CTXA- and QCT-derived mechanical properties at FN. The Bland-Altman plot of CTXA- and QCT-derived shear stiffness has similar pattern with that of axial stiffness due to the linear relation between elasticity and shear modulus since the Poisson's ration is assumed as a constant in this study. Therefore, shear stiffness Bland-Altman plot is not displayed. As shown in Figure 5.2, CTXA derived mechanical properties slightly underestimate those derived by QCT. Around 95% points are inside the 95% confidence interval and the distance between the upper and lower margins is clinically acceptable. Also, the variability, especially in Figure 5.2 (c), is around the mean constant (others are not so clear probably due to the small sample size). Therefore, a fairly good agreement between the CTXA and QCT derived mechanical properties can be concluded, which may justify the use of two dimensional CTXA in replacement of three dimensional QCT in assessing femur bone quality. However, there indeed exist non-trivial differences between CTXA- and QCT-derived parameters. The main reason may come from the relation between the elasticity and bone mineral density, which is nonlinear in this study. Also, the cross-section used to calculate the stiffness in CTXA and QCT may not be the same one due to the various errors, e.g., the software operator, the quality of the images, the difference of algorithm to locate the interested cross-section between CTXA and QCT image. Finally, considering the fact that bone mechanical properties depend on many factors and testing conditions, the measurement to establish the relation between the elasticity and bone mineral density used in this study may also be a contributor to the difference in CTXA and QCT derived stiffness.

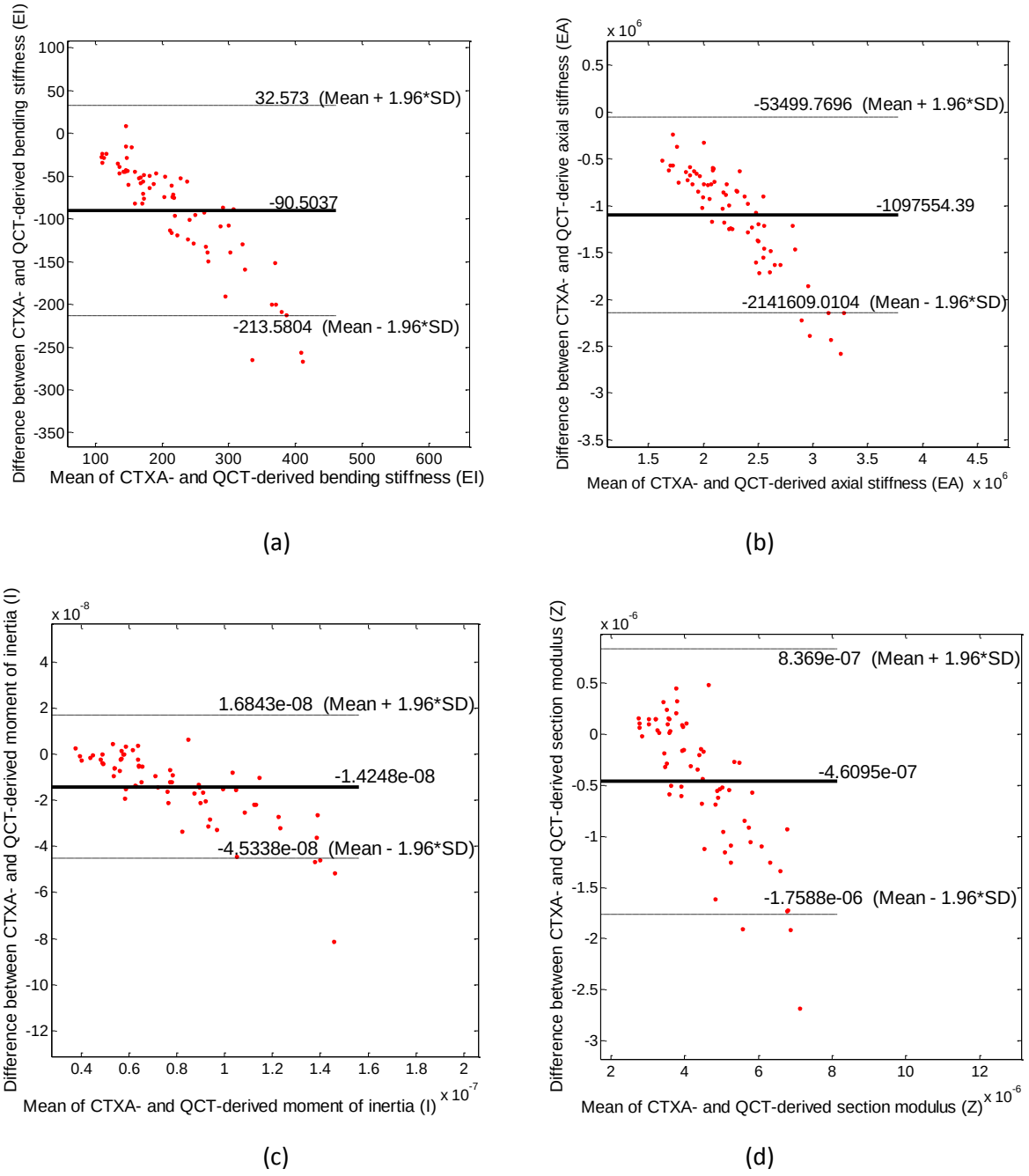

Figure 5.2 Bland-Altman plot of CTXA- and QCT- derived stiffness. (a) Bending stiffness at FN; (b) Axial stiffness at FN; (c) Moment of inertia at FN; (d) Section modulus at FN

5.3.3 Establishment of Equivalence between QCT- and DXA- Based Cross-sectional Stiffness

From the results shown in the above sections, it can be seen that there exist very strong correlations and great consistency between CTXA- and QCT- derived femur cross-section stiffness. Therefore, it can be reasonably concluded that CTXA-derived stiffness parameters are equivalent to those computed from QCT images. As know, CTXA is equivalent to DXA [77, 78]. This means CTXA is a bridge which connect DXA and QCT, as shown in Figure 5.3. Therefore, the stiffness derived from DXA image are equivalent to those derived from QCT image, which means two dimensional DXA derived cross-section stiffness can be used to replace three dimensional QCT derived cross-section stiffness in evaluating bone quality.

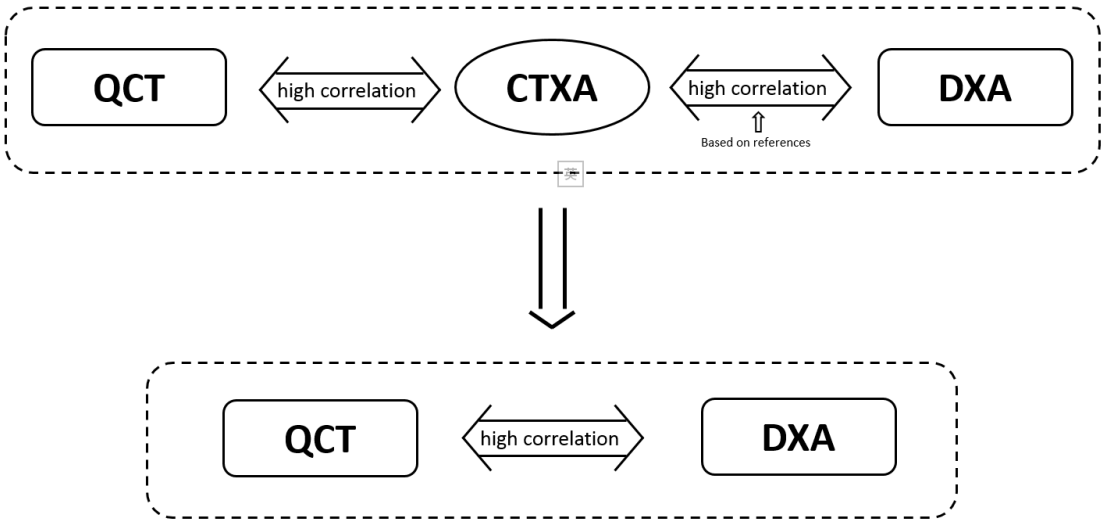

Figure 5.3 The relations among QCT, CTXA and DXA derived cross-sectional stiffness

5.4 Study on the Possible Effect of PPI on BMD

Proton pump inhibitors (PPIs) are the most potent agents used for gastric acid suppression. PPIs are now one of the most prescribed medications in clinic [106, 107]. However, over the past decade, there have been an increasing number of studies indicating there is an association between the long-term use of PPIs and the development of hip fracture [108-115]. The strengths of the associations differ considerably from study to study. Some research supported that PPI use is associated with the development of low bone mineral density which can be diagnosed as osteoporosis or reason of fracture [116-121]. On the other hand, other research argued that PPI use does not have a significant effect on bone mineral loss [106, 108, 122-130]. Actually, the lack of a definitive physiologic mechanism through which PPI use would negatively affect bone mineral density strongly support this view. Based on Laura E. Targownik et al [106], further studies are required to demonstrate PPI-associated hip fracture risk.

This section will conduct the analysis through SPSS software to examine if it is possible to discriminate PPI users from non-PPI users through the cross-sectional stiffness, BMD, and FRI based on the 2-D beam model, and give another support that PPI is associated with either the presence of osteoporosis or accelerated BMD loss. AUC, the area under the ROC (receiver operating characteristic) curve is employed to measure the accuracy of the methods to correctly classify the PPI users and non-PPI users. A rough guide for the accuracy level is defined as [131]

0.9-1=excellent; 0.8-0.9=good; 0.7-0.8=fair; 0.6-0.7=poor; 0.5-0.6=fail.

5.4.1 Discrimination of PPI Use based on the cross-sectional stiffness

Ninety-two cases were used to validate if PPI use is associated with decreased bone quality, including 47 controls and 45 PPI users. Table 5.5 shows the accuracy of cross-sectional stiffness in discriminating the PPI users and the non-PPI users. As shown in Table 5.5, the AUC are all around 0.5. Based on the guide for the accuracy level, the cross-sectional stiffness failed to correctly classify those with and without taking PPIs. This result tells us PPI does not affect bone quality.

Table 5.5 AUC of stiffness in discriminating PPIs user from non-PPIs user

Stiffness	Cross-section	AUC
EI	FN	0.553
	IT	0.531
	FS	0.517
EA	FN	0.518
	IT	0.528
	FS	0.553

5.4.2 Discrimination of PPI Use based on BMD

Table 5.6 shows the accuracy of bone mineral density (BMD) to determine the associations of PPI use with bone mineral density (BMD). As we can see, the AUC is around 0.5, which means it is worthless to use BMD to discriminate PPI users from non-PPI users. From these results, it can be conclude that PPI use does not affect the bone mineral density.

Table 5.6 AUC of BMD in discriminating PPIs user from non-PPIs user

Bone density	Cross-section	AUC
BMD	FN	0.504
	IT	0.530
	FS	0.573

5.4.3 Discrimination of PPI Use based on FRI

Recent studies raised the concern that patients on PPIs are at increased risk of hip fractures. In this study, hip fracture risk index (FRI) was calculated by simulating two normal loading conditions: sideways fall and one-legged stance. AUC (area under the ROC curve) was calculated to examine the effects of PPI use on the development of osteoporosis-related fractures, and the results are shown in Table 5.7. As shown in Table 5.7, the AUC (area under the ROC curve) of FRI at the three critical cross-sections based on the two loading conditions are all around 0.5. That suggests that FRI cannot discriminate PPI users from non-PPI users. Therefore, there is no association of PPI use with hip bone fractures.

To sum up, the cross-sectional stiffness, BMD, and FRI cannot discriminate the PPI user from non-PPI user, which means there is no significant association between use of PPIs and the presence of osteoporosis or accelerated BMD loss. This supports the point of view that PPI does not lead to an increased occurrence of BMD loss or hip bone fractures.

Table 5.7 AUC of FRI in discriminating PPIs user from non-PPIs user

FRI	Cross-section	AUC
Sideways Fall	FN	0.549
	IT	0.536
	FS	0.551
Single Leg	FN	0.555
	IT	0.531
	FS	0.556

Chapter 6

Conclusion and Recommendation of Future Work

Hip fracture is a serious public health problem and a major cause of suffering, disability, and death among elderly people, which has imposed significant burden on community healthcare systems. A fast, accurate and effective evaluation of hip fracture risk is essential for accurate health care planning and establishing proper treatments. Therefore, the applicability and the universal availability are required for a clinical assessment technique. In this study, the equivalence between CTXA- and QCT-derived femur cross-section stiffness was established, which can justify the use of DXA in replacement of QCT in assessing femur bone quality. After that, a subject specific CTXA-derived beam model, combing with CTXA-derived femur cross-section stiffness, was developed to assess hip fracture risk during the sideways fall and single-leg stance loading configurations, respectively. Finally, it is verified that if PPI use is associated with the presence of osteoporosis or accelerated BMD loss based on cross-sectional stiffness, BMD and FRI.

6.1 Conclusion and Contributions

A total of 92 clinical cases were obtained from Winnipeg Health Science Centre for this study. It has been found that QCT-derived stiffness, namely, bending stiffness, axial stiffness, and shearing stiffness are highly correlated with CTXA-derived stiffness, which means the equivalence between 3-D and 2-D image based cross-section stiffness can be built. CTXA could provide the same clinical utility as that afforded by DXA [77], therefore, the use of DXA in replacement of QCT in assessing femur bone quality could be partially justified. It has been demonstrated that the cross-sectional stiffness, BMD, and FRI cannot discriminate the PPI users from non-PPI users, which gives the support that PPI use is not associated with the presence of osteoporosis or accelerated BMD loss. However, some procedures, such as the guideline of subject position in QCT scanning and the development of image techniques in improving image quality, should be implemented to improve the accuracy of the statistical analysis.

The main contributions from the current study are summarized as follows:

1. A novel method, known as cross-section stiffness, to evaluate bone quality is proposed. Bone material property and bone geometry are considered, which is more accuracy and reasonable in engineering point of view.
2. The equivalence between CTXA and QCT derived femur cross-section stiffness is built, which helps to justify the use of DXA in replacement of QCT in assessing femur bone quality.
3. A semi-automatic contour extraction of the proximal femur is created in this study. Individual information including bone property and bone geometry, and the loading conditions are consider into the beam model to simulate the real world situation.

4. A 2-D CTXA based beam model was constructed to calculate the hip fracture risk index (FRI) in cooperation with the CTXA-derived femur cross-section stiffness, which can be easily implemented into clinical practice.
5. The test of discrimination between PPI users and non-PPI users based on cross-sectional stiffness, BMD and FRI is conducted, and gives the support that PPI use is not associated with the presence of osteoporosis or accelerated BMD loss.

6.2 Future Work

In the following list, some recommendations are suggested for the future works which may perfect this whole project.

1. The neutral axis of the femur bone cross-section needs to be located in the calculation of the cross-section stiffness in order to make the results more accuracy.
2. The accuracy of the beam model will be studied in discriminating clinic fracture cases from controls, and in comparing with those of other biomechanical models, for example, DXA-based FE model;
3. The effect of material models on the correlations between CTXA and QCT derived cross-sectional stiffness will be investigated to obtain the most suitable models.
4. An automatic and optimized contour extraction of the femur will be developed in order to decrease the errors.
5. The techniques of image processing will be improved to eliminate as much as possible the errors caused by the image quality.
6. A well-developed material model will be applied to the cortical bone and trabecular bone respectively in order to improve the accuracy of the cross-section stiffness.

Bibliography

[1] O. Johnell and J. Kanis. An estimate of the worldwide prevalence and disability associated with osteoporotic fractures. *Osteoporosis international*, 17(12):1726–1733, 2006.

[2] T. Kehler. Epidemiology of osteoporosis and osteoporotic fractures. *Reumatizam*, 61(2):60–64, 2014.

[3] C. Cooper, E. J. Atkinson, S. J. Jacobsen, W. M. O'Fallon, and L. J. Melton. Population-based study of survival after osteoporotic fractures. *American journal of epidemiology*, 137(9):1001–1005, 1993.

[4] C. L. Leibson, A. Tosteson, S. E. Gabriel, J. E. Ransom, and L. J. Melton. Mortality, disability, and nursing home use for persons with and without hip fracture: a population-based study. *Journal of the American Geriatrics Society*, 50(10):1644–1650, 2002.

[5] J. Magaziner, E. Lydick, W. Hawkes, K. M. Fox, S. I. Zimmerman, R. S. Epstein, and J. R.. Hebel. Excess mortality attributable to hip fracture in white women aged 70 years and older. *American Journal of Public Health*, 87(10):1630–1636, 1997.

[6] J. Magaziner, E. M. Simonsick, T. M. Kashner, J. R. Hebel, and J. E. Kenzora. Predictors of functional recovery one year following hospital discharge for hip fracture: a prospective study. *Journal of Gerontology*, 45(3):M101–M107, 1990.

[7] P. Spiegel. Osteoporosis, etiology, diagnosis, and management. *Journal of Orthopaedic Trauma*, 10(3):220, 1996.

[8] L.J. Melton. Hip fractures: a worldwide problem today and tomorrow. *Bone*, 14:1–8, 1993.

[9] S. R. Cummings and L. J. Melton. Epidemiology and outcomes of osteoporotic fractures. *The Lancet*, 359(9319):1761–1767, 2002.

[10] B. Lentle, A. M. Cheung, D. A. Hanley, W. D. Leslie, D. Lyons, A. Papaioannou, S. Atkinson, J. P. Brown, S. Feldman, A. B. Hodsman, et al. Osteoporosis Canada 2010 guidelines for the assessment of fracture risk. *Canadian Association of Radiologists Journal*, 62(4):243–250, 2011.

[11] A. Singer, A. Exuzides, L. Spangler, C. O'Malley, C. Colby, K. Johnston, I. Agodoa, J. Baker, and R. Kagan. Burden of illness for osteoporotic fractures compared with other serious diseases among postmenopausal women in the United States. In *Mayo Clinic Proceedings*, 90(1):53–62, 2015.

[12] J.E. Tarride, R.B. Hopkins, W.D. Leslie, S. Morin, J.D. Adachi, A. Papaioannou, L. Bessette, J.P. Brown, and R. Goeree. The burden of illness of osteoporosis in Canada. *Osteoporosis International*, 23(11):2591–2600, 2012.

[13] L.J. Melton. Epidemiology of hip fractures: implications of the exponential increase with age. *Bone*, 18(3):S121–S125, 1996.

[14] J. A. Grisso, J. L. Kelsey, B. L. Strom, G. Y. Ghiu, G. Maislin, L. A. O'Brien, S. Hoffman, and F. Kaplan. Risk factors for falls as a cause of hip fracture in women. *New England Journal of Medicine*, 324(19):1326–1331, 1991.

[15] S. N. Robinovitch, L. Inkster, J. Maurer, and B. Warnick. Strategies for avoiding hip impact during sideways falls. *Journal of Bone and Mineral Research*, 18(7):1267–1273, 2003.

[16] C. Cooper and L. J. Melton. Epidemiology of osteoporosis. *Trends in Endocrinology & Metabolism*, 3(6):224–229, 1992.

[17] C. Cooper, G Campion, and L.J. Melton. Hip fractures in the elderly: a world-wide projection. *Osteoporosis International*, 2(6):285–289, 1992.

[18] B. Gullberg, O. Johnell, and J.A. Kanis. World-wide projections for hip fracture. *Osteoporosis International*, 7(5):407–413, 1997.

[19] K. J. Koval and J. D. Zuckerman. Economics of hip fracture treatment. In *Hip Fractures*, 303–312, 2000.

[20] R. Goeree, B. O'Brien, D. Pettitt, L. Cuddy, M. Ferraz, and J. Adachi. An assessment of the burden of illness due to osteoporosis in canada. *Journal-Sogc*, 18:15–24, 1996.

[21] E. A. Papadimitropoulos, P. C. Coyte, R. G. Josse, and C. E. Greenwood. Current and projected rates of hip fracture in Canada. *Canadian Medical Association Journal*, 157(10):1357–1363, 1997.

[22] S.A. Jackson, A. Tenenhouse, L. Robertson, et al. Vertebral fracture definition from population-based data: preliminary results from the Canadian multicenter osteoporosis study (camos). *Osteoporosis International*, 11(8):680–687, 2000.

[23] J. B. Lauritzen. Hip fractures: incidence, risk factors, energy absorption, and prevention. *Bone*, 18(1):S65–S75, 1996.

[24] C. Christodoulou and C. Cooper. What is osteoporosis? *Postgraduate Medical Journal*, 79(929):133–138, 2003.

[25] J.E. Tarride, R.B. Hopkins, W.D. Leslie, S. Morin, J.D. Adachi, A. Papaioannou, L. Bessette, J.P. Brown, and R. Goeree. The burden of illness of osteoporosis in Canada. *Osteoporosis International*, 23(11):2591–2600, 2012.

[26] J. A. Stevens and S. Olson. Reducing falls and resulting hip fractures among older women. *Home Care Provider*, 5(4):134–141, 2000.

[27] B. Hagsten, O. Svensson, and A. Gardulf. Health-related quality of life and self-reported ability concerning ADL and IADL after hip fracture: a randomized trial. *Acta Orthopaedica*, 77(1):114–119, 2006.

[28] K. J. Koval and J. Zuckerman. Hip fractures: a practical guide to management. *Springer Science & Business Media*, 2000.

[29] L. C. Brunner, L. E. Oates, and T. Y. Kuo. Hip fractures in adults. *American Family Physician*, 67(3):537–542, 2003.

[30] J. D. Michelson, A. Myers, R. Jinnah, Q. Cox, and M. V. Natta. Epidemiology of hip fractures among the elderly: Risk factors for fracture type. *Clinical Orthopaedics and Related Research*, 311:129–135, 1995.

[31] M. Butler, M. Forte, R. .L Kane, S. Joglekar, S. J. Duval, M. Swiontkowski, and T. Wilt. *Treatment of common hip fractures*. Agency for Healthcare Research and Quality, 2009.

[32] F. Cosman, S.J. De Beur, M.S. LeBoff, E.M. Lewiecki, B. Tanner, S. Randall, and R. Lindsay. Clinician guide to prevention and treatment of osteoporosis. *Osteoporosis International*, 25(10):2359–2381, 2014.

[33] J. A. Kanis, E. V. McCloskey, H. Johansson, A. Oden, L. J. Melton, and N. Khaltaev. A reference standard for the description of osteoporosis. *Bone*, 42(3):467–475, 2008.

[34] K. Siminoski, W. D. Leslie, H. Frame, A. Hodsman, R. G. Josse, A. Khan, B. C. Lentle, J. Levesque, D. J. Lyons, G. Tarulli, et al. Recommendations for bone mineral density reporting in Canada: a shift to absolute fracture risk assessment. *Journal of Clinical Densitometry*, 10(2):120–123, 2007.

[35] S. E. Brown. Bone density tests aren't enough. Why a fracture risk assessment is essential. http://www.betterbones.com/testing/bone-density-tests-arent-enough/.

[36] N. B Watts, E. M. Lewiecki, P. D. Miller, and S. Baim. National osteoporosis foundation 2008 clinician's guide to prevention and treatment of osteoporosis and the world health organization fracture risk assessment tool (frax): what they mean to the bone densitometrist and bone technologist. *Journal of Clinical Densitometry*, 11(4):473–477, 2008.

[37] J. A. Kanis, F. Borgstrom, C. De Laet, H. Johansson, O. Johnell, B. Jonsson, A. Oden, N. Zethraeus, B. Pfleger, and N. Khaltaev. Assessment of fracture risk. *Osteoporosis International*, 16(6):581–589, 2005.

[38] J. A. Kanis, O. Johnell, C. De Laet, B. Jonsson, A. Oden, and A. K. Ogelsby. International variations in hip fracture probabilities: implications for risk assessment. *Journal of Bone and Mineral Research*, 17(7):1237–1244, 2002.

[39] W.C. Hayes. Prediction of femoral impact forces in falls on the hip. *Age, 24: 30, 1991*.

[40] T. J. Beck, C. B. Ruff, K. E. Warden, W. W. Scott Jr, and G. U. Rao. Predicting femoral neck strength from bone mineral data: a structural approach. *Investigative Radiology*, 25(1):6–18, 1990.

[41] T. J. Beck. Extending dxa beyond bone mineral density: understanding hip structure analysis. *Current Osteoporosis Reports*, 5(2):49–55, 2007.

[42] J.K. Brown, Q. Qiao, J. Weigert, B.C.C. Khoo, and T.J. Beck. Improved precision of hip structure analysis using optimized projection images from segmented 3d CT scans of the hip. *J Bone Miner Res*, 20(Suppl 1):S337, 2005.

[43] N.J. Crabtree, H. Kroger, A. Martin, H.A.P. Pols, R. Lorenc, J. Nijs, J.J. Stepan, J.A. Falch, T. Miazgowski, and S. Grazio, et al. Improving risk assessment: hip geometry, bone mineral distribution and bone strength in hip fracture cases and controls. the epos study. *Osteoporosis International*, 13(1):48–54, 2002.

[44] W. C. Hayes, S.J. Piazza, and P.K. Zysset. Biomechanics of fracture risk prediction of the hip and spine by quantitative computed tomography. *Radiologic Clinics of North America*, 29(1):1–18, 1991.

[45] Y. Luo. A biomechanical sorting of clinical risk factors affecting osteoporotic hip fracture. *Osteoporosis International*, pages 1–17, 2015.

[46] A. B. Dufour, B. Roberts, K. E. Broe, D. P. Kiel, M. L. Bouxsein, and M. T. Hannan. The factor-of-risk biomechanical approach predicts hip fracture in men and women: the framingham study. *Osteoporosis International*, 23(2):513–520, 2012.

[47] Y. Luo, Z. Ferdous, and W.D. Leslie. A preliminary dual-energy x-ray absorptiometry-based finite element model for assessing osteoporotic hip fracture risk. *Proceedings of the Institution of Mechanical Engineers, Part H: Journal of Engineering in Medicine*, 225(12):1188-1195, 2011.

[48] L. B. Arey, W. Burrows, J.P. Greenhill, and R. M. Hewitt. Dorland's illustrated medical dictionary. *The American Journal of the Medical Sciences*, 234(6):733, 1957.

[49] E. S. Orwoll, L. M. Marshall, C. M. Nielson, S. R. Cummings, J. Lapidus, J. A. Cauley, K. Ensrud, N. Lane, P. R. Hoffmann, D. L. Kopperdahl, et al. Finite element analysis of the proximal femur and hip fracture risk in older men. *Journal of Bone and Mineral Research*, 24(3):475–483, 2009.

[50] K. Kroemer, S. Snook, S. Meadows, and S. Deutsch. Ergonomic models of anthropometry, human biomechanics and operator-equipment interfaces. 1988.

[51] H.W. H. Poort, T.J.J.H. Thomas Slooff, et al. A new method to analyse the mechanical behaviour of skeletal parts. *Acta Orthopaedica Scandinavica*, 43(5):301-317,1972.

[52] R. Huiskes and E.Y.S. Chao. A survey of finite element analysis in orthopedic biomechanics: the first decade. *Journal of Biomechanics*, 16(6):385–409, 1983.

[53] J.C. Lotz, E.J. Cheal, and W.C. Hayes. Fracture prediction for the proximal femur using finite element models: part I linear analysis. *Journal of Biomechanical Engineering*, 113(4):353–360, 1991.

[54] J.C. Lotz, E.J. Cheal, and W.C. Hayes. Fracture prediction for the proximal femur using finite element models: part ii nonlinear analysis. *Journal of Biomechanical Engineering*, 113(4):361–365, 1991.

[55] P. K. Zysset, E. Dall'Ara, P. Varga, and D.H. Pahr. Finite element analysis for prediction of bone strength. *Bone Key Reports*, 2, 2013.

[56] D. Testi, M. Viceconti, F. Baruffaldi, and A. Cappello. Risk of fracture in elderly patients: a new predictive index based on bone mineral density and finite element analysis. *Computer Methods and Programs in Biomedicine*, 60(1):23–33, 1999.

[57] J. O. D. Buijs and D. D. Daescu. Validated finite element models of the proximal femur using two-dimensional projected geometry and bone density. *Computer Methods and Programs in Biomedicine*, 104(2):168–174, 2011.

[58] J. H. Keyak, T. S. Kaneko, J. Tehranzadeh, and H. B. Skinner. Predicting proximal femoral strength using structural engineering models. *Clinical Orthopaedics and Related Research*, 437:219–228, 2005.

[59] M. Viceconti, L. Bellingeri, L. Cristofolini, and A. Toni. A comparative study on different methods of automatic mesh generation of human femurs. *Medical Engineering & Physics*, 20(1):1–10, 1998.

[60] D. D. Cody, G. J. Gross, F. J. Hou, H. J. Spencer, S. A. Goldstein, and D. P. Fyhrie. Femoral strength is better predicted by finite element models than qct and dxa. *Journal of Biomechanics*, 32(10):1013–1020, 1999.

[61] K. Imai. Computed tomography-based finite element analysis to assess fracture risk and osteoporosis treatment. *World Journal of Experimental Medicine*, 5(3):182, 2015.

[62] M. Mirzaei, M. Keshavarzian, and V. Naeini. Analysis of strength and failure pattern of human proximal femur using quantitative computed tomography (QCT)-based finite element method. *Bone*, 64:108–114, 2014.

[63] E. Dall'Ara, B. Luisier, R. Schmidt, F. Kainberger, P. Zysset, and D. Pahr. A nonlinear qct-based finite element model validation study for the human femur tested in two configurations in vitro. *Bone*, 52(1):27–38, 2013.

[64] M. Bessho, I. Ohnishi, J. Matsuyama, T. Matsumoto, K. Imai, and K. Nakamura. Prediction of strength and strain of the proximal femur by a ct-based finite element method. *Journal of Biomechanics*, 40(8):1745–1753, 2007.

[65] M. Bessho, I. Ohnishi, T. Matsumoto, S. Ohashi, J. Matsuyama, K. Tobita, M. Kaneko, and K. Nakamura. Prediction of proximal femur strength using a ct-based nonlinear finite element method: differences in predicted fracture load and site with changing load and boundary conditions. *Bone*, 45(2):226–231, 2009.

[66] J.H. Keyak. Improved prediction of proximal femoral fracture load using nonlinear finite element models. *Medical Engineering & Physics*, 23(3):165–173, 2001.

[67] D. Testi, M. Viceconti, F. Baruffaldi, and A. Cappello. Risk of fracture in elderly patients: a new predictive index based on bone mineral density and finite element analysis. *Computer Methods and Programs in Biomedicine*, 60(1):23–33, 1999.

[68] Y. Luo, Z. Ferdous, and W. D. Leslie. Precision study of DXA-based patient-specific finite element modeling for assessing hip fracture risk. *International Journal for Numerical Methods in Biomedical Engineering*, 29(5):615–629, 2013.

[69] M. E. Danielson, T. J. Beck, A. S. Karlamangla, G. A. Greendale, E. J. Atkinson, Y. Lian, A. S. Khaled, T. M. Keaveny, D. Kopperdahl, K. Ruppert, et al. A comparison of DXA and CT based methods for estimating the strength of the femoral neck in post-menopausal women. *Osteoporosis International*, 24(4):1379–1388, 2013.

[70] B. V. Rietbergen, R. Huiskes, F. Eckstein, and P. Rüegsegger. Trabecular bone tissue strains in the healthy and osteoporotic human femur. *Journal of Bone and Mineral Research*, 18(10):1781–1788, 2003.

[71] E. Verhulp, B. V. Rietbergen, and R. Huiskes. Comparison of micro-level and continuum-level voxel models of the proximal femur. *Journal of Biomechanics*, 39(16):2951–2957, 2006.

[72] E.F. Rybicki, F.A. Simonen, and E.B. Weis. On the mathematical analysis of stress in the human femur. *Journal of Biomechanics*, 5(2):203–215, 1972.

[73] E. P. Salathe, G. A. Arangio, and E. P. Salathe. An application of beam theory to determine the stress and deformation of long bones. *Journal of Biomechanics*, 22(3):189–199, 1989.

[74] D.D. Raftopoulos and W. Qassem. Three-dimensional curved beam stress analysis of the human femur. *Journal of Biomedical Engineering*, 9(4):356–366, 1987.

[75] L. Yang, N. Peel, J. A. Clowes, E. V. McCloskey, and R. Eastell. Use of DXA-based structural engineering models of the proximal femur to discriminate hip fracture. *Journal of Bone and Mineral Research*, 24(1):33–42, 2009.

[76] F. A. Mourtada, T. J. Beck, D. L. Hauser, C. B. Ruff, and G. Bao. Curved beam model of the proximal femur for estimating stress using dual-energy x-ray absorptiometry derived structural geometry. *Journal of Orthopaedic Research*, 14(3):483–492, 1996.

[77] C. E. Cann, J. E. Adams, J. K. Brown, and A. D. Brett. CTXA hip- an extension of classical DXA measurements using quantitative CT. *PloS one*, 9(3):e91904, 2014.

[78] B.C.C Khoo, K. Brown, C. Cann, K. Zhu, S. Henzell, V. Low, S. Gustafsson, R.I. Price, and R.L. Prince. Comparison of QCT-derived and DXA-derived areal bone mineral density and t scores. *Osteoporosis International*, 20(9):1539–1545, 2009.

[79] Wikipe. Femur structure. https://en.wikipedia.org/wiki/Femur.

[80] Zoology. Femur structure. http://www.zoology.ubc.ca/ biomania/tutorial/bonesk/anc13.htm.

[81] B. Helgason, E. Perilli, E. Schileo, F. Taddei, S. Brynjólfsson, and M. Viceconti. Mathematical relationships between bone density and mechanical properties: a literature review. *Clinical Biomechanics*, 23(2):135–146, 2008.

[82] D. C. Wirtz, N. Schiffers, T. Pandorf, K. Radermacher, D. Weichert, and R. Forst. Critical evaluation of known bone material properties to realize anisotropic FE-simulation of the proximal femur. *Journal of Biomechanics*, 33(10):1325–1330, 2000.

[83] G. Guglielmi and T. F. Lang. Quantitative computed tomography. In *Seminars in Musculoskeletal Radiology*, 6: 219–227, 2002.

[84] Mindways Sofware. CTXA hip BMD application module. http://qct.com/home/products/.

[85] E. Schileo, E. Dall, F. Taddei, A. Malandrino, T. Schotkamp, M. Baleani, and M. Viceconti. An accurate estimation of bone density improves the accuracy of subject-specific finite element models. *Journal of Biomechanics*, 41(11):2483–2491, 2008.

[86] J. C. Villa-Camacho, O. Iyoha-Bello, S. Behrouzi, B. D. Snyder, and A. Nazarian. Computed tomography-based rigidity analysis: a review of the approach in preclinical and clinical studies. *BoneKEy Reports*, 3, 2014.

[87] D. C. Wirtz, N. Schiffers, T. Pandorf, K. Radermacher, D. Weichert, and R. Forst. Critical evaluation of known bone material properties to realize anisotropic fe-simulation of the proximal femur. *Journal of Biomechanics*, 33(10):1325–1330, 2000.

[88] C. E. Cann, J. E. Adams, J. K. Brown, and A. D. Brett. CTXA hip-an extension of classical DXA measurements using QCT. *Journal of Bone and Mineral Research*, 18: 317–S317, 2003.

[89] B. C.C. Khoo, T. J. Beck, Q. Qiao, P. Parakh, L. Semanick, R. L. Prince, K.P. Singer, and R. I. Price. In vivo short-term precision of hip structure analysis variables in comparison with bone mineral density using paired dual-energy x-ray absorptiometry scans from multi-center clinical trials. *Bone*, 37(1):112–121, 2005.

[90] S. V. Cauter, M. D. Beule, A. V. Haver, P. Verdonk, and B. Verhegghe. Automated extraction of the femoral shaft axis and its distal entry point from full and reduced 3D models. In *3rd ECCOMAS Thematic conference on Computational Vision and Medical Image Processing (VipIMAGE 2011)*, 57–61, 2011.

[91] B. C.C. Khoo, T. J. Beck, Q. Qiao, P. Parakh, L. Semanick, R. L. Prince, K. P. Singer, and R. I. Price. In vivo short-term precision of hip structure analysis variables in comparison with bone

mineral density using paired dual-energy x-ray absorptiometry scans from multi-center clinical trials. *Bone*, 37(1):112–121, 2005.

[92] Y. Luo, H. Yang, L. Targownik, A. Goertzen, and W. D. Leslie. A preliminary study of dxa and qct derived femur cross-section stiffness. In *Applied Mechanics and Materials*, . 775: 415–419, 2015.

[93] M. R. Feldesman, J. G. Kleckner, and J. K. Lundy. Femur/stature ratio and estimates of stature in mid-and late-pleistocene fossil hominids. *American Journal of Physical Anthropology*, 83(3):359–372, 1990.

[94] S. L. Greenspan, E.R. Myers, D. P. Kiel, R. A. Parker, W. C. Hayes, and N. M. Resnick. Fall direction, bone mineral density, and function: risk factors for hip fracture in frail nursing home elderly. *The American Journal of Medicine*, 104(6):539–545, 1998.

[95] M. Sinaki. Falls, fractures, and hip pads. *Current Osteoporosis Reports*, 2(4):131–137, 2004.

[96] U. Roy, M. Kowshik, A. Ganguly, N. Nath, P. Mane, H. Chelladurai, R. Narayan, and S. Bhand. List of projects completed under certain project-oriented courses in the year 2009 (goa campus).

[97] T. Yoshikawa, C.H. Turner, M. Peacock, C.W. Slemenda, C.M. Weaver, D. Teegarden, P. Markwardt, and D.B. Burr. Geometric structure of the femoral neck measured using dual-energy x-ray absorptiometry. *Journal of Bone and Mineral Research*, 9(7):1053–1064, 1994.

[98] A. Rohlmann, U. Mössner, G. Bergmann, and R. Kölbel. Finite-element-analysis and experimental investigation of stresses in a femur. *Journal of Biomedical Engineering*, 4(3):241–246, 1982.

[99] S.N. Robinovitch, W.C. Hayes, and T.A. McMahon. Prediction of femoral impact forces in falls on the hip. *Journal of Biomechanical Engineering*, 113(4):366–374, 1991.

[100] E. Schileo, F. Taddei, L. Cristofolini, and M. Viceconti. Subject-specific finite element models implementing a maximum principal strain criterion are able to estimate failure risk and fracture location on human femurs tested in vitro. *Journal of Biomechanics*, 41(2):356–367, 2008.

[101] T. Ota, I. Yamamoto, and R. Morita. Fracture simulation of the femoral bone using the finite-element method: how a fracture initiates and proceeds. *Journal of Bone and Mineral Metabolism*, 17(2):108–112, 1999.

[102] J. H. Keyak and S. A. Rossi. Prediction of femoral fracture load using finite element models: an examination of stress-and strain-based failure theories. *Journal of Biomechanics*, 33(2):209–214, 2000.

[103] J. Cordei and E. Gautier. Strain gauges used in the mechanical testing of bones. part i: Theoretical and technical aspects. *Injury, International Journal of the Care of the Injured*, 30(1):7–13, 1999.

[104] T. S. Keller. Predicting the compressive mechanical behavior of bone. *Journal of Biomechanics*, 27(9):1159–1168, 1994.

[105] E. F. Morgan, H. H. Bayraktar, and T. M. Keaveny. Trabecular bone modulus–density relationships depend on anatomic site. *Journal of Biomechanics*, 36(7):897–904, 2003.

[106] L. E. Targownik, W. D. Leslie, K. S. Davison, D. Goltzman, S. A. Jamal, N. Kreiger, R. G. Josse, S. M. Kaiser, C. S. Kovacs, J. C. Prior, et al. The relationship between proton pump inhibitor use and longitudinal change in bone mineral density: a population-based from the canadian multicentre osteoporosis study (camos). *The American Journal of Gastroenterology*, 107(9):1361–1369, 2012.

[107] J. P. Reilly. Safety profile of the proton-pump inhibitors. *American Journal of Health-system Pharmacy*, 56(4):11–17, 1999.

[108] W. Y. Elaine, T. Blackwell, K. E. Ensrud, T. A. Hillier, N. E Lane, E. Orwoll, and D. C. Bauer. Acid-suppressive medications and risk of bone loss and fracture in older adults. *Calcified Tissue International*, 83(4):251–259, 2008.

[109] L. E. Targownik. Therapy: Another bad break for proton-pump inhibitors? *Nature Reviews Rheumatology*, 5(9):478–480, 2009.

[110] C. Roux, K. Briot, L. Gossec, S. Kolta, T. Blenk, D. Felsenberg, D. M. Reid, R. Eastell, and C. C. Glüer. Increase in vertebral fracture risk in postmenopausal women using omeprazole. *Calcified Tissue International*, 84(1):13–19, 2009.

[111] Y. Yang, J. D. Lewis, S. Epstein, and D. C. Metz. Long-term proton pump inhibitor therapy and risk of hip fracture. *Jama*, 296(24):2947–2953, 2006.

[112] D. A. Corley, A. Kubo, W. Zhao, and C. Quesenberry. Proton pump inhibitors and histamine-2 receptor antagonists are associated with hip fractures among at-risk patients. *Gastroenterology*, 139(1):93–101, 2010.

[113] P. Vestergaard, L. Rejnmark, and L. Mosekilde. Proton pump inhibitors, histamine h2 receptor antagonists, and other antacid medications and the risk of fracture. *Calcified Tissue International*, 79(2):76–83, 2006.

[114] S. Pouwels, A. Lalmohamed, P. Souverein, C. Cooper, B.J. Veldt, H.G. Leufkens, A. Boer, T. V. Staa, and F. D. Vries. Use of proton pump inhibitors and risk of hip/femur fracture: a population-based case-control study. *Osteoporosis International*, 22(3):903–910, 2011.

[115] H. Khalili, E. S. Huang, B. C. Jacobson, C. A. Camargo, D. Feskanich, and A. T. Chan. Use of proton pump inhibitors and risk of hip fracture in relation to dietary and lifestyle factors: a prospective cohort study. *BMj*, 344:372, 2012.

[116] R. R. Recker. Calcium absorption and achlorhydria. *New England Journal of Medicine*, 313(2):70–73, 1985.

[117] M. J. Wright, D. D. Proctor, K. L. Insogna, and J.E. Kerstetter. Proton pump-inhibiting drugs, calcium homeostasis, and bone health. *Nutrition Reviews*, 66(2):103–108, 2008.

[118] R. Gagnemo-Persson, R. Håkanson, F. Sundler, and P. Persson. Growth of the parathyroid glands in omeprazole-treated chickens. *Scandinavian Journal of Gastroenterology*, 29(6):493–497, 1994.

[119] L. Grimelius, H. Johansson, G. Lundqvist, A. Olazabal, J.H. Polak, and A.G.E. Pearse. The parathyroid glands in experimentally induced hypergastrinemia in the rat. *Scandinavian Journal of Gastroenterology*, 12(6):739–744, 1977.

[120] G.L. Cui, U. Syversen, C.M. Zhao, D. Chen, and H.L. Waldum. Long-term omeprazole treatment suppresses body weight gain and bone mineralization in young male rats. *Scandinavian Journal of Gastroenterology*, 36(10):1011–1015, 2001.

[121] T. Schinke, A. F. Schilling, A. Baranowsky, S. Seitz, R. P. Marshall, T. Linn, M. Blaeker, A. K. Huebner, A. Schulz, R. Simon, et al. Impaired gastric acidification negatively affects calcium homeostasis and bone mass. *Nature Medicine*, 15(6):674–681, 2009.

[122] G. W. Bo-Linn, G. R. Davis, D. J. Buddrus, S. G. Morawski, C. S. Ana, and J. S. Fordtran. An evaluation of the importance of gastric acid secretion in the absorption of dietary calcium. *Journal of Clinical Investigation*, 73(3):640, 1984.

[123] G. Graziani, S. Badalamenti, G. Como, M. Gallieni, S. Finazzi, C. Angelini, D. Brancaccio, and C. Ponticelli. Calcium and phosphate plasma levels in dialysis patients after dietary ca-p overload. *Nephron*, 91(3):474–479, 2002.

[124] M. J. Wright, R. R. Sullivan, E. Gaffney-Stomberg, D. M. Caseria, K. O. O'Brien, D. D. Proctor, C. A. Simpson, J. E. Kerstetter, and K.L. Insogna. Inhibiting gastric acid production does not affect intestinal calcium absorption in young, healthy individuals: a randomized, crossover, controlled clinical trial. *Journal of Bone and Mineral Research*, 25(10):2205–2211, 2010.

[125] J. Tuukkanen and H.K. Väänänen. Omeprazole, a specific inhibitor of h+- k+-atpase, inhibits bone resorptionin vitro. *Calcified Tissue International*, 38(2):123–125, 1986.

[126] P. Moayyedi and A. Cranney. Hip fracture and proton pump inhibitor therapy: balancing the evidence for benefit and harm. *The American Journal of Gastroenterology*, 103(10):2428–2431, 2008.

[127] L. E. Targownik, L. M. Lix, S. Leung, and W. D. Leslie. Proton-pump inhibitor use is not associated with osteoporosis or accelerated bone mineral density loss. *Gastroenterology*, 138(3):896–904, 2010.

[128] K. L. Insogna. The effect of proton pump-inhibiting drugs on mineral metabolism. *The American Journal of Gastroenterology*, 104:2–4, 2009.

[129] Y. Yang. Proton pump inhibitor therapy and osteoporosis. *Current Drug Safety*, 3(3):204–209, 2008.

[130] L. Laine. Proton pump inhibitors and bone fractures&quest. *The American Journal of Gastroenterology*, 104:S21–S26, 2009.

[131] Gim. Auc. http://gim.unmc.edu/dxtests/roc3.htm.